Winter 11-15-2018

MANTLE-TO-SURFACE NEOTECTONIC CONNECTIONS IN THE SAN JUAN MOUNTAINS DOCUMENTED BY 3HE/4HE, CO2 FLUX MEAUREMENTS, AND HYDROCHEMICAL ANALYSIS OF THE GEOTHERMAL SYSTEM NEAR RICO, COLORADO

Benjamin D. Holt
University of New Mexico - Main Campus

Benjamin Holt

Candidate

Earth and Planetary Sciences

Department

This thesis is approved, and it is in acceptable quality and form for publication:

Approved by the Thesis Committee:

_____, Chairperson

_____

_____

_____

MANTLE-TO-SURFACE NEOTECTONIC CONNECTIONS IN THE SAN JUAN MOUNTAINS DOCUMENTED BY $^{3}HE/^{4}HE$, CO_2 FLUX MEAUREMENTS, AND HYDROCHEMICAL ANALYSIS OF THE GEOTHERMAL SYSTEM NEAR RICO, COLORADO

BY

BENJAMIN HOLT

BACHELOR OF SCIENCE, THE OHIO STATE UNIVERSITY

THESIS

Submitted in Partial Fulfillment of the

Requirements for the Degree of

Master of Science

Master of Science in Earth and Planetary Science

The University of New Mexico

Albuquerque, New Mexico

December, 2018

Mantle-to-surface Neotectonic Connections in the San Juan Mountains Documented by $^{3}He/^{4}He$, CO_2 Flux Measurements and Hydrochemical Analysis of the Geothermal System near Rico, Colorado

Benjamin Holt

Bachelor of Science, The Ohio State University

Master of Science, University of New Mexico

ABSTRACT

This project investigates the controls on geothermal fluids and their conduit systems which may account for high mantle helium components of geothermal fluids in intracratonic continental regions. The field laboratory is the western San Juan Mountains of southwestern Colorado where the structural setting and hydrochemistry of carbonic springs suggest potential connections among surface hot springs, fault networks, CO_2 degassing, significant geothermal potential, young volcanic and plutonic rocks (< 7 Ma), and low-velocity upper mantle. The Rico Hot Springs have the highest mantle volatile component of any spring in Colorado with air-corrected values of $^{3}He/^{4}He = 5.88\ R_A$ indicating 73% mantle helium component. This near-MORB mantle helium value at Rico indicates that volatiles degassing from the mantle must be rapidly transmitted into the groundwater system along deep-seated faults such that accumulation of ^{4}He from radiogenic crust has not swamped mantle-derived primordial ^{3}He. Geologic features that are important for volatile transport and spring chemistry controls include a complex conduit system and fault network involving the Precambrian-cored Rico Dome, ~4 Ma intrusive rocks at Calico Peak and Priest Gulch, and a low-velocity upper mantle. Therefore, Rico and the surrounding region is a natural laboratory for studying geothermal fluid and mantle volatile pathways. Additional noble gas analyses and

hydrochemistry data were gathered from regional springs and modeled via chemical geothermometers. New noble gas measurements from this study, paired with literature values, reveal highest air corrected $^{3}He/^{4}He$ at Rico (4.09-5.88 R_A), Dunton (3.11-4.54 R_A), Geyser Warm Spring (3.39 R_A), and Paradise Warm Spring (2.72 R_A). Water volume is dominated by meteoric fluids as shown by stable isotope data but hydrochemistry indicates high TDS, high CO_2, and high He come from a geothermal fluid endmember. Variable mixing and water-rock interactions are processes that can explain chemistry variations between spatially proximal springs. CO_2 flux measurements (up to 36.2 $g/m^2/hr$) vary across structural features and demonstrate that the faults act as pathways for CO_2 flux suggesting ongoing degassing. Overall, we find that local high mantle helium signature is localized directly above regions of lowest upper mantle velocity in the San Juan mantle anomaly and is derived from neotectonic mantle melts in those regions.

TABLE OF CONTENTS

LIST OF FIGURES

LIST OF TABLES

Introduction

Geothermal systems provide opportunities for development of geothermal energy and commercial CO_2 gas fields, study of fluid mixing and impacts on water quality, and analysis of the regional carbon budget. Western U.S. geothermal systems are of particular interest because they record diffuse degassing of mantle volatiles into the near-surface groundwater systems in springs (termed "continental smokers") (Crossey et al., 2015). These mantle-to-surface connections and resultant spring chemistries are varied, complex, and incompletely understood. Furthermore, the characterization of the mantle signature at these springs can be applied to identify regions of active mantle degassing and provide insight into mantle dynamics.

This paper builds on the regional study of Colorado hot springs by Karlstrom et al. (2013) and Easley and Morgan (2013) by focusing on the geothermal springs of the western San Juan Mountains (WSJ). The WSJ springs were chosen as the field laboratory for investigation of mantle-to-surface conduits due to the anomalously high mantle signature measured at the Rico hot springs (73% MORB) (Easley and Morgan, 2013). The goal of this study is to improve our understanding of this anomalous signature, and thereby our understanding of geothermal fluid conduit systems and what their mantle signature tells us about mantle dynamics. Figure 1 shows a general map of this study area and the geothermal springs investigated in this paper.

We apply multiple geochemical tracers to improve our understanding of the hydrochemistry of geothermal springs and geometry of their conduit systems. Tracers applied to both new and published data include helium isotope data, major and trace elemental analysis, including geothermal tracers, and stable isotopes. Hydrochemical data are used to determine chemistries of individual springs (on a Piper diagram), to apply chemical geothermometry, and to help identify the degree of mixing between springs versus isolated circulation pathways. Stable isotopes help elucidate the relative meteoric and endogenic components of each spring. Noble gas chemistry is assessed to resolve the components of mantle, crustal, and atmospheric gas in spring samples. Spatial changes in CO_2 flux were measured around the Rico Hot Springs to refine mapping of the structures associated with these springs in the near-surface.

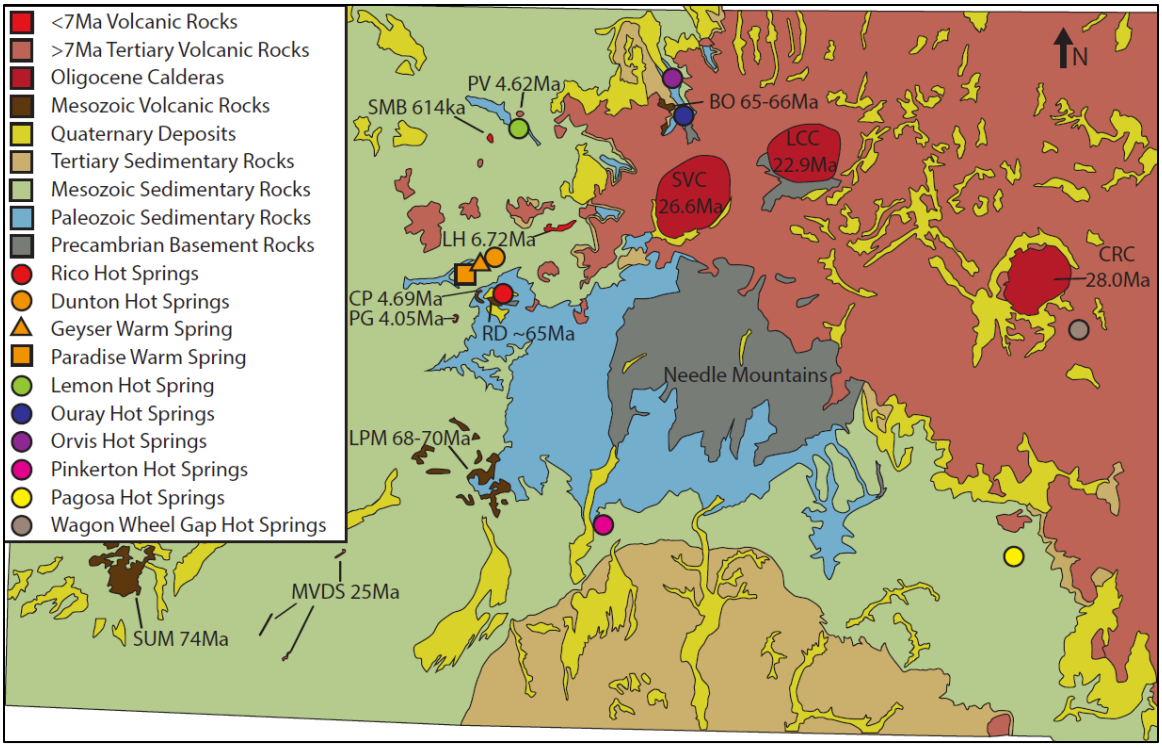

Figure 1. Geothermal springs in context of volcanism grouped by age throughout the San Juans. A general trend is seen of youngest volcanism in the westernmost San Juans. Previous 3He/4He measurements have been made by previous studies at Wagon Wheel Gap, Pagosa, Pinkerton, Orvis, Ouray, Rico, and Geyser spring (Table 2). The data gaps and presence of youngest volcanism in the westernmost San Juans piqued our interest in this area. Adapted from Gonzales, 2017. (Abbreviations: BO=Blowout Stock, CP=Calico Peak, CRC=Creede Caldera, LCC=Lake City Caldera, LH=Lizard Head Peak, LPM=La Plata Mtns, MVDS=Mesa Verde Dike Swarm, PG=Priest Gulch Stock, PV=Placerville Minette Dikes, RD=Rico Dome, SMB=Specie Mesa Basalt, SUM=Sleeping Ute Mtn, SVC=Silverton Caldera)

Our results provide new insights into the source and transport pathways for geothermal gas and fluids and the ways they affect groundwater. At the broadest scale, the results are compared to mantle tomography which lets us observe connections between mantle dynamics and groundwater composition. A summary of young magmatism is given for understanding of crustal pathways. At the most localized scale, spatial volatile flux measurements lead to a refined understanding of the nearest-surface component of these mantle-to-surface pathways. Overall, the combination of these complementary methods and new data in the context of existing data, regional geology, and mantle dynamics results in a deepened understanding of these fascinating and important systems.

Background

Helium isotopes, specifically $^3He/^4He$ ratios, are a powerful tool for detection of mantle gas signature due to both their inert nature and the distinctive sources for each isotope. ^3He is the primordial isotope of Helium that was created during the formation of the solar system, then sequestered in the deep Earth, and since has steadily degassed from the mantle (Clarke et al, 1969). In contrast, ^4He accumulates in the crust and atmosphere from radioactive decay of common crustal elements such as U, Th, and K (Andrews, 1985). An elevated $^3He/^4He$ ratio indicates the presence of mantle gas at the surface and suggests relatively rapid mantle-to-surface conduit systems because this ratio decreases as fluid spends more time in contact with crustal rocks accumulating ^4He. The measured $^3He/^4He$ ratio (R_m or R) is commonly reported as a factor relative of R_A, where R_A is $^3He/^4He$ ratio of the atmosphere (1.38×10^{-6}). A correction (R_C) is made to account for any atmospheric contamination based on the He/Ne and He/Ar ratios (Hilton, 1995; Boles et al, 2015). This framework for reporting $^3He/^4He$ ratios allows us to establish several important endmember values. On the low end, a value of 0.02 R_A or less is representative of continental crust and considered to have no significant mantle signature (Andrews, 1985). In contrast, values 0.1 R_A or greater in non-air-like groundwater indicate significant mantle helium contributions (Clarke et al., 1969). High endmembers of mantle helium are defined by the MORB value of ~8 R_A, and values >30 R_A can be observed at plumes (Lupton, 1983; Graham, 2002). CO_2 is considered to be the main carrier gas for mantle helium such that $CO_2/^3He$ is useful as an additional tracer. MORB values of $CO_2/^3He$ are $\sim 2 \times 10^9$, with crustal values ranging up to 5 orders of magnitude higher.

Figure 2 shows published data for $^3He/^4He$ in Colorado hot springs plotted relative to mantle velocity at 80-km depth (Karlstrom et al., 2013). This study proposed a correlation between domains of low P-wave velocity (indicative of the presence of partial melt) and higher $^3He/^4He$ values at surface springs. One of the goals of the present study is to continue to test this correlation and to examine the concept that high $^3He/^4He$ in hot springs is the surface manifestation of mantle-to-surface conduit systems and reflects

ongoing mantle neotectonics that may also be related to young uplift of the Colorado Plateau.

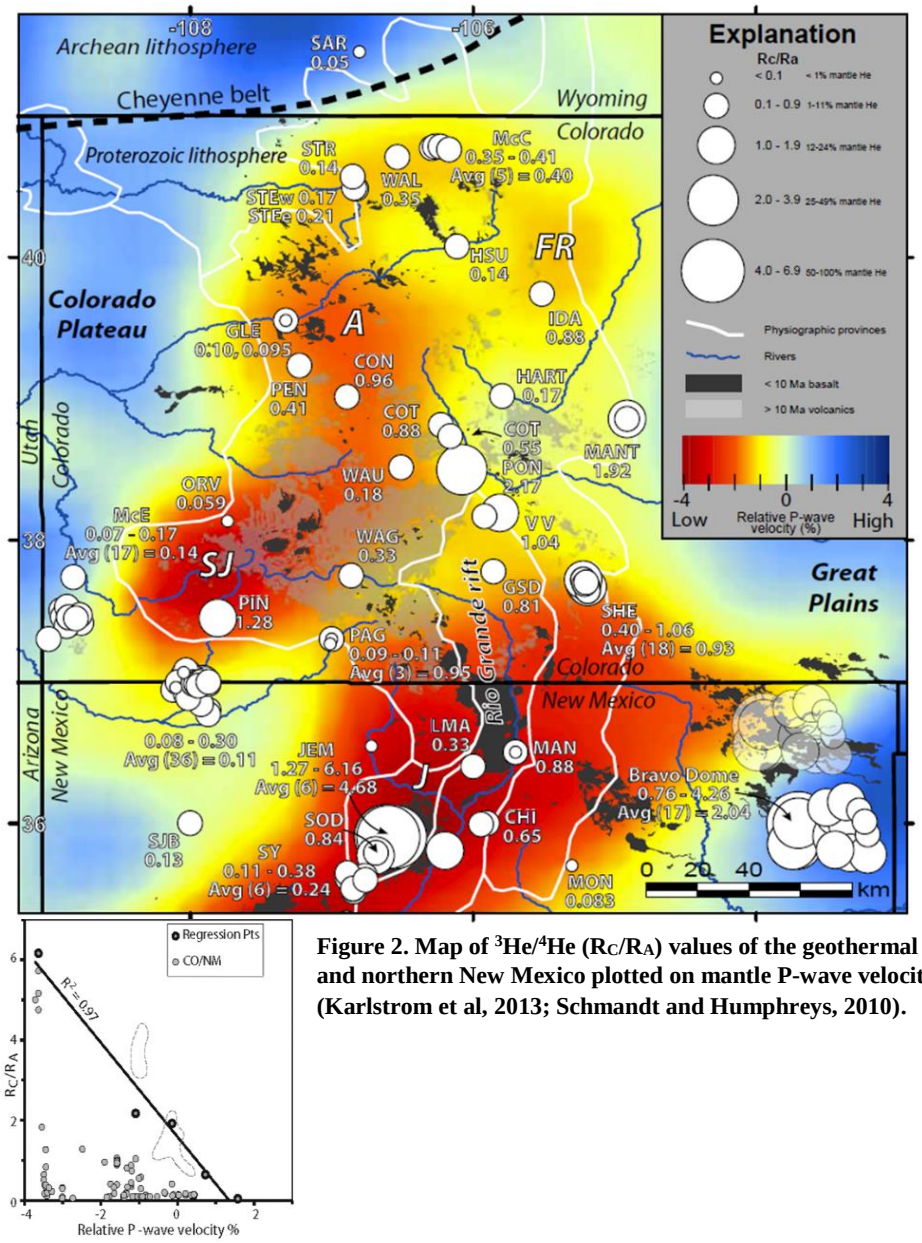

Figure 2. Map of $^{3}He/^{4}He$ (R_C/R_A) values of the geothermal springs in Colorado and northern New Mexico plotted on mantle P-wave velocity at 80-km depth (Karlstrom et al, 2013; Schmandt and Humphreys, 2010).

The western San Juan Mountains (WSJ) is a key area to study hot springs and geothermal potential for several reasons. The $^{3}He/^{4}He$ value of 5.88 R_A (73% mantle helium) found at the Rico Hot Springs (Easley and Morgan, 2013) is the highest value found in Colorado and rivals values up to 6.16 R_A at the 1.25 Ma Valles Caldera system in New Mexico (Fig. 2). Also, young magmatism is now recognized in this region that includes both 6.8-3.4 Ma felsic intrusions and basalts as young as 614 ka (Gonzales, 2015; Gonzales, 2017). In addition, the western slope is interpreted to be uplifting due to

mantle buoyancy change (Karlstrom et al., 2012; Rosenburg et al., 2014). Also, existing measurements such as 0.06 R_A at Orvis (Karlstrom et al, 2013) reveal a wide variation in mantle contributions to hot springs such that this region provides a natural laboratory for studying fluid mixing to explain the wide range of values and for investigating whether there is a significant association between mantle helium anomalies and major faults, other structural features, and/or young volcanism (Hoke et al, 2000; Craddock et al, 2017; Gonzales et al., 2016).

Geologic setting

Geology of the San Juan Mountains

The San Juan Mountains is one of the highest elevation, highest relief areas of Colorado. Its geologic evolution includes formation of basement 1.8-1.6 billion years ago (Karlstrom et al., 2017), faulting and erosional exhumation of middle crustal rocks to the surface before the Cambrian to form the Great Unconformity, and Paleozoic and Mesozoic sedimentation including generally thinned sections in the lower Paleozoic, variable thickness Pennsylvanian sections related to Ancestral Rockies uplifts, (Thomas 2007), early Mesozoic terrestrial environments and the Cretaceous inland seaway (Raynolds and Hagadorn, 2015). Cenozoic uplift history involved several stages of uplift: initial departure from sea level during the ~ 70 Ma Laramide orogeny; surface uplift related to development of the 38-23 Ma San Juan volcanic field; and post-10 Ma uplift related to young magmatism and mantle buoyancy modifications (Karlstrom et al., 2012). The relative uplift amounts during each event are debated. Hansen et al. (2013) showed that highest topography in the San Juans is underlain by relatively thin crust (< 45 km) compared to surrounding areas such that topography is supported by a combination of buoyant crust and buoyant upper mantle. These data seem best explained by delamination of dense restitic lower crust during and after caldera-related magmatism followed by mantle convection and asthenospheric upwelling such that there is a likely genetic connection between magmatism, uplift history, and the numerous ore deposits and geothermal systems.

Cenozoic magmatic history also involved the same 3 stages. Laramide (65-70 Ma) magmatism included parts of the Colorado Mineral Belt (Mutchler et al. 1987), and laccoliths in the Navajo volcanic filed that was dominated by felsic to intermediate calc-alkaline intrusions (Gonzales, 2015). During the Oligocene, the Farallon Slab of the Laramide Orogeny began to delaminate and rollback (Ricketts et al., 2016). Regional extension likely began at this time which caused melting of the subcontinental lithosphere beneath the San Juans and a resultant surge of volcanism called the Oligocene Ignimbrite Flare-Up from approximately 35-23Ma. This period is marked by both emplacement of plutons of intermediate to felsic magma as well as the formation of caldera complexes at Silverton, Lake City, and Creede. Mid-Tertiary magmatism in the WSJ was 30-20 Ma and involved caldera eruptions, high volume rhyolitic ignimbrite eruptions in the San Juan Mountains, and mafic to felsic stocks and porphyries in the Rico area. Post-10-Ma magmatism included relatively small plutons in the Rico area. These included the 6.72 Ma Lizard Head minette dike, 4.62 Ma Placerville minette dikes, 4.7 Ma Calico Peak latite porphyry stock and dikes, and 4.1 Priest Gulch monzonite sill. These are granodiorite plutons that are unlikely to have been emplaced at depths less than 3-5 km such that their presence at the surface reflects several km of exhumation of the Rico area in the past 3-5 Ma. The youngest magmatism involved scattered basaltic eruptions between 7 and 0.6 Ma (Gonzales, 2017). The youngest volcanic rock in the region is the 614ka Specie Mesa basalt flow near Placerville and Lemon Spring (Gonzales, 2017). In this paper, we consider regional hot springs as a potential continued record of regional volcanism in the sense that these vents transport heat, mantle-derived fluids, and volatiles from depth (Fig. 3).

The history of faulting is long and complex. Regional uplift from the Laramide Orogeny introduced complex fault networks such as the Rico dome that often penetrate basement rocks and likely reactivated cryptic basement structures. Overturned beds and N-dipping thrust faults suggest that Rico Dome was initially a Laramide S-facing monoclinal structure. Faulting in the past 10 Ma is known in Colorado, but is not yet documented in the region. However, the reverse fault system in the Rico Dome includes normal faults that we interpret to be Miocene reactivated Laramide faults as discussed

below. The presence of hot springs along older faults shows that the fault network acts as fluid conduits and also raises the possibility of young extensional slip.

Mineralization of note that may represent prior incarnations of the Rico geothermal system include the Pliocene Silver Creek molybdenum porphyry deposit and epigenic gold deposits. Both of these ores occur as veins and replacement deposits, where the molybdenum deposits are associated with the hornblende latite porphyry while the gold deposits are primarily within the Hermosa Formation. The mineralization throughout the Rico district are all associated with a 4Ma hydrothermal system in the region (McKnight, 1974; Larson et al, 1994a) that we view as the precursor to the Rico hot springs system.

Geologic setting of hot springs in the western San Juans

Rico

Figure 4 shows a generalized geologic map of the Rico area (Pratt et al., 1969). There are three hot springs at Rico located in a cluster with two on the East side of the Dolores River and the other one on the West side. We use the naming of Oerter (2011) to label these Rico #1, 2, and 3 (Fig. 4). The dominant structural feature of this study area is the Rico Dome, a Precambrian-cored uplift that exposes a Paleoproterozoic greenstone, the Uncompahgre Quartzite, and Proterozoic hornblende diorite (McKnight, 1974; Pratt, 1969). Basement rocks are overlain by Mississippian, Pennsylvanian and Permian strata and then by Quaternary surficial deposits. Rico Dome has an E-W hinge axis and is proposed to be originally of Laramide age based on its monoclonal geometry; it was also inferred to be of Laramide age based on the assignment of the Rico monzonite as Laramide (McKnight, 1974; Gonzales, 2015; Gonzales, 2017). However, new dating suggests Tertiary ages for some Rico area intrusive rocks (Gonzales, 2017; as suspected by Pratt et al., 1969) and these plutons are offset indicating younger fault movement as well. Magmatism took place in the core of the Rico dome in the form of 3.4-3.9Ma alaskite porphyry and 6.8Ma hornblende latite (Gonzales, 2015).

Figure 3. Gas sampling at Rico #1 (bottom left), view of Rico #2 pool (top), and view of Rico #3 (bottom right)

All three springs are located in a fault block on the monoclonal north side of Rico Dome within lower Paleozoic strata that have been down-dropped along the east-trending Last Chance fault relative to Precambrian basement to the south but that has been upthrown relative to younger Paleozoic strata along the N-dipping east-trending Nellie

Bly fault to the north (Pratt et al, 1969). We interpret the original geometry to be that of a Laramide S-verging anticlinal structure above an inferred N-dipping basement fault system that cores Rico Dome, with Miocene normal reactivation of older faults.

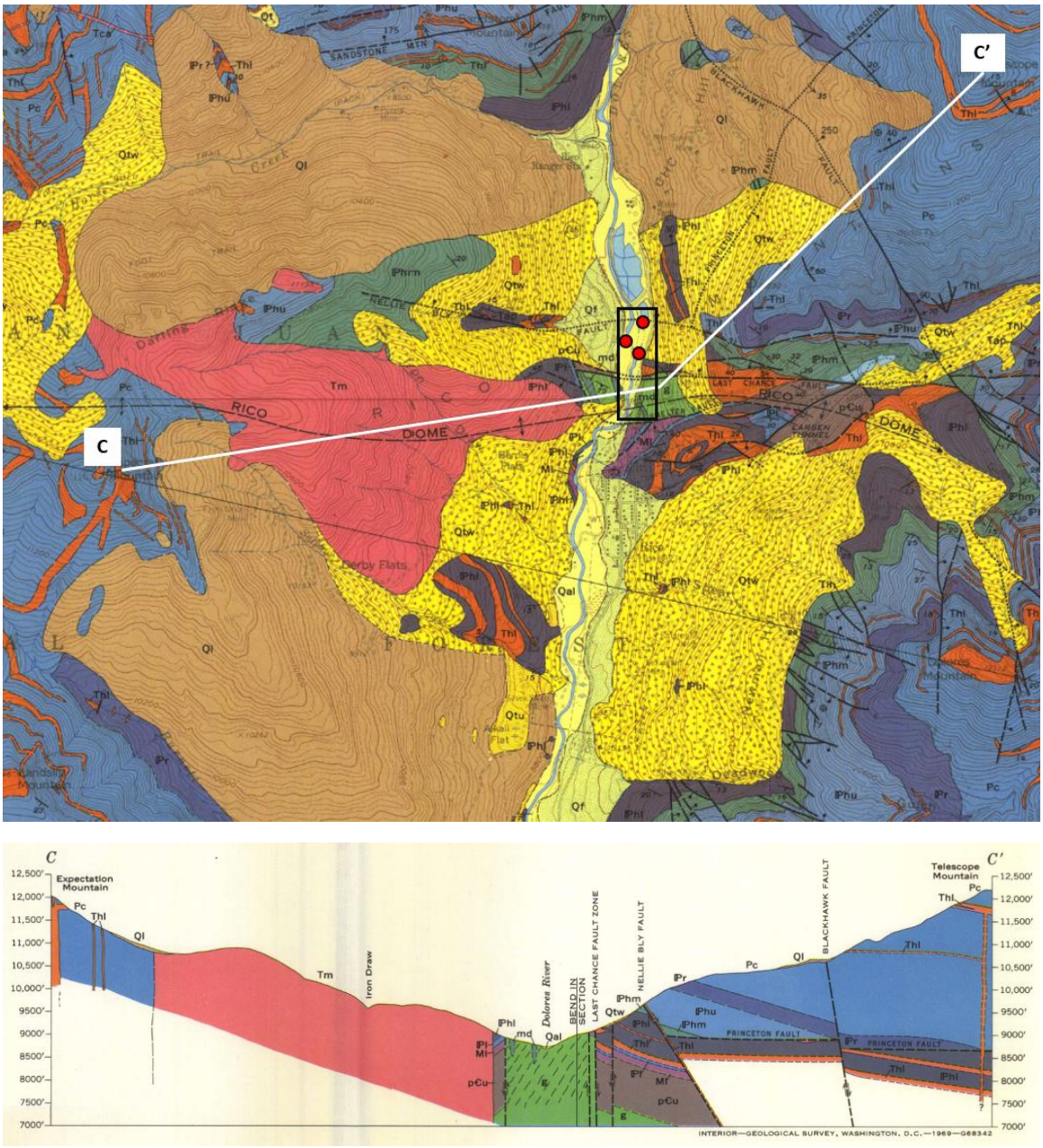

Figure 4. Geologic map and cross section of the Rico, Colorado area, modified from Pratt et al, 1969. The Precambrian-cored Rico Dome trends roughly E-W and is bounded by steeply N-dipping faults. Although in a covered interval of Dolores River alluvial valley fill, Rico hot springs (red dots) are interpreted to occur in Paleozoic strata on the dipping N-limb of Rico Dome between two major E-W trending normal faults, the Last Chance and Nellie Bly. Two N-S CO_2 flux transects were measured within the area marked by the black box (see Figure 7).

Lemon Warm Spring

The area surrounding Placerville exhibits complex fault geometry since it is in the transition zone between the Uncompahgre Plateau and La Plata Mountains. The spring itself is inside a tunnel within the Dolores Formation which it flows out of and into a surface pool (Fig. 5). A large north-trending and smaller northeast-trending fault intersect and terminate at the spring site (Bush et al, 1956). This fault intersection likely creates a high permeability point and preferential flow path for these spring waters from depth. Lemon is considered a warm spring as its waters are only 31 to 33 degrees Celsius (Barrett and Pearl, 1978). This spring is notably located about 2 miles north of the youngest extrusive igneous rocks in the area, the 614ka Specie Mesa basalt (Gonzales et al, 2017).

Figure 5. Outlet of Lemon Spring during February, 2017 sampling. Spring itself discharges within the cave.

Dunton, Geyser, and Paradise Hot Springs

Dunton, Geyser, and Paradise hot springs are discussed together because they all occur within 2.5 miles of one another along the West Fork of the Dolores River. The Dunton hot springs are located about 10 km (6 miles) NW of Rico and are at an elevation of 2705 m (8873 feet), just along the bank of the West Fork of the Dolores River. The

primary surface bedrock of this area and at the Dunton hot spring vent is the red sandstones and shales the Triassic Dolores Formation. Unlike Rico's E-W faults and dome structure, the area surrounding Dunton is dominated by N-S and NW-SE trending faults. The Dunton hot spring itself is located along a Miocene N-S fault which is approximately parallel to a local syncline and brings the Jurassic Morrison Formation into contact with older units of the Dolores and Jurassic Entrada Formations (Barrett and Pearl, 1978; Bush and Bromfield, 1966). The trail to Geyser Warm Spring begins 3km downstream of Dunton Spring. Geyser Warm Spring itself is at an elevation of 2940 m (9643 feet) as it is located on a hillslope slightly less than a mile SE of the river itself. Geyser distinguishes itself from the other springs in this study by being the only spring with geyser action in the state of Colorado. This action occurs in roughly 30 minute cycles, its periodicity is difficult to constrain as it is only expressed is a minor change in the intensity of bubbling on the spring surface. In contrast to Dunton, this spring occurs where a NW-SE fault terminates at its intersection with a large NE-SW trending fault. Paradise Warm Spring is at an elevation of 2610 m (8563 feet) and is located within a bath house along the river another 0.3 mile downstream of Geyser Warm Spring trailhead. Detailed mapping of geologic structure has still not been done in this area. However, due to its proximity to Geyser Warm Spring, it is likely that this spring is also controlled by NE-SW and NW-SE fault interaction. All three of these springs emerge from the Dolores Formation at the surface (Bush and Bromfield, 1966).

Figure 6. Runoff pool of spring water outside of Dunton Resort (left), bath house containing Paradise spring (top right), and Geyser Warm spring showing minor geyser action (bottom right).

Methods

Noble gas methods

To understand regional mantle signature variation, this study first collected samples for helium isotope analysis at four regional hot springs which have not been previously measured (Lemon, Dunton, Paradise, Geyser). Duplicate samples were also collected from the springs at Rico, Ouray, and Orvis. Gas samples were collected at the same time as water samples, with the exceptions Geyser, Box Canyon in Ouray, and duplicate samples at Rico. Duplicate samples of springs previously measured in the literature were collected to test whether existing R_A values accurately record variation in mantle signatures. Samples were collected in a copper tube by using an apparatus consisting of a funnel connected to plastic tubing, the copper tube, and exhaust plastic tubing. The funnel is held down into the rising gas from the spring which then flows through the system. This continues for about 3 minutes to fully flush atmospheric gas from the copper tube. Then, metal Swagelock clamps are tightened on both ends of the

copper tube. These clamps form a “cold weld” in which the malleable copper seals prevent helium escape. Samples were sent to the Water, Energy, and Life Laboratory at The Ohio State University for analysis by Dr. Thomas Darrah and PhD student Colin Whyte.

Hydrochemistry methods

Hydrochemical analyses allow us to make interpretations about water-rock interactions, source of spring fluids, spring mixing and circulation pathways, and geothermometry. Pairing these analyses with contemporaneous gas samples, we are also able to make interpretations about the extent to which the geothermal fluid and gas pathways are coupled. We gathered 17 new samples from Rico, Dunton, Geyser, Paradise, Lemon, Ouray, and Orvis Hot Springs and these were synthesized with a comprehensive dataset of over 300 previous water analyses from Colorado geothermal springs.

Water sampling was performed following the techniques detailed in the USGS National Field Manual for the Collection of Water-Quality Data (2006). Water samples were gathered at Lemon, Dunton, Paradise, Geyser, Orvis, Wiesbaden, and Box Canyon springs as well as at each of the three Rico Hot Springs (Fig. 1). Field parameters of temperature, pH, and specific conductance, were measured in the field using an Oakton waterproof pH/CON 300 meter. At each site, at least two samples were collected. Both were filtered (0.45µm) and one was acidified using HNO_3. These samples were then processed for alkalinity, major ion, and stable isotope geochemistry. The alkalinity measurements were determined using the procedures in Michalowski et al., (2012). Inductively coupled plasma optical emission spectroscopy and ion chromatography were used to determine major ion chemistry using the methods from Hou and Jones (2000) and Jackson (2000) respectively.

Several analytical techniques were applied to this data such that we could have a robust multiple-tracer approach to water chemistry interpretations. Oxygen isotopes have been utilized to determine the extent to which spring fluids are sourced from rapidly

circulating meteoric waters and/or from geothermal brines with a longer residence time (e.g. Powell and Cumming, 2010). Trace elements and salts were measured as another way to see if spring fluids have a substantial component of geothermal brines and assess potential water-rock interactions (Crossey et al, 2009). Analysis of major cations and anions are plotted on a Piper diagram (Piper, 1944). This graph summarizes the chemistry of all the springs of interest on one figure, which allows for evaluation of the extent of mixing between regional spring fluids along their circulation pathways as well as possible water-rock interactions. Using the spreadsheet from Powell and Cumming, 2010, we generated geothermometry estimates and compared them to estimates from previous studies (Oerter, 2011; Smith et al, 2018; Easley and Morgan, 2013; Barrett and Pearl, 1978) to better characterize potential geothermal resources.

CO_2 flux measurements

CO_2 flux is a powerful tool for understanding mantle-surface connections because CO_2 is the primary carrier gas for mantle helium to surface systems (Marty and Jambon, 1987). CO_2 in Colorado hot springs is overwhelmingly endogenic (deep-sourced) (Karlstrom et al, 2013). Therefore, surface measurements of high CO_2 flux in our study area likely reveal the presence of high-permeability zones and deep fault networks which provide a mantle-to-surface volatile pathway (Lewicki and Brantley, 2000; Werner et al., 2008; Crossey et al., 2009; Smith, 2016). This is particularly useful because high topography, alluvial fill, and dense plant cover often make direct observation of geologic structures difficult near hot springs in the WSJ. In such settings, the use of CO_2 flux measurements provides a way to observe geologic structures that are conduits for gas transport as well as measure the rate of gas diffusion along those structures. Furthermore, along these faults which transport travertine-depositing fluids, high CO_2 flux shows that permeability of these transport networks is likely maintained by recent tectonic fracturing (Chiodini et al., 2007), which serve as another signal of regional neotectonic activity.

This study used the hand-held PP-systems EGM-5 CO_2 flux meter (Chiodini et al, 1998). The system is flushed with background air for several seconds before each measurement. After this, the cylindrical accumulation chamber is put on the ground and held firmly in place for the measurement interval. CO_2 flux is measured by the change in

CO_2 concentration over a two-minute period. However, the measurement will end before the entire two minutes has elapsed if maximum flux or concentration has been reached in that time. In these cases, the EGM-5 will report an estimate flux value will be generated by fitting a function to the data gathered before the measurement period stops. During use, air entering the system passes through an internal hydrophobic filter to protect the analyzer from water damage. From there, the input gas is pumped to an infrared gas analyzer which yields concentrations of CO_2. The EGM-5 reports the raw concentration as well as change in concentration over the measurement interval. These concentrations are fit to both linear and quadratic functions to report both linear and quadratic flux estimates for each point (in $g/m^2/hr$). Most samples had fairly constant rates of CO_2 accumulation over the measurement interval, and therefore the linear flux rates are used in our data analysis.

This technique was applied near the Rico Hot Springs so that we could refine mapping of and observe degassing related to three primary E-W trending mapped structures proximal to the springs. These are the Nellie Bly Fault, Last Chance Fault, and Rico Dome (discussed in the geologic setting of Rico above) (Fig. 4). Over 200 measurements were taken along two transects at Rico, located on the east and west banks of the Dolores River near the three hot springs. These transects ran N-S and each cross the Nellie Bly Fault, Last Chance Fault, the Rico Dome to determine their prominence as degassing sources and volatile transport mechanisms for the Rico Hot Springs. Most of measurements taken along the eastern transect were taken on dirt next to the road that runs up the northernmost of the Rico Hot Springs. However, most of the values on the western transect were measured in dense vegetation which itself has a biogenic component of CO_2 degassing (Crossey, 2009; Smith, 2016). To constrain the influence of daily plant respiration cycles, we took soil CO_2 flux measurements in the morning, afternoon, and evening at 3 points in the field site with densely vegetated ground cover. At the same times, we also measured air samples to establish the background atmospheric CO_2 levels.

Results

Helium isotopes

Results of helium isotope analyses are reported in Table 1. Significant mantle helium was measured in all of our samples from the WSJ. The highest R_A values were measured at the Rico Hot Springs, ranging from 4.09 to 5.88 R_A which is comparable to the previously measured 5.88R_A value (Easley and Morgan, 2013). Several of the springs which previously had not been measured for helium isotopes yielded the next highest mantle signatures in the region. These notable values were from Dunton Hot Spring (3.11-4.55 R_A), Geyser Warm Spring (3.39), and Paradise Warm Spring (2.72 R_A). Lemon Hot Spring also yielded significant mantle signature, with a value of 0.95 R_A.

Sample Name	Spring name	Source	Latitude	Longitude	R/R_A	R_c/R_A	$CO_2/^3He$	^4He	Ne	He/Ne	% Mantle
Rico-1 22617	**Rico Hot Springs**	**this study**	**37.70193**	**-108.03115**	**4.09**	**4.09**	**6.76E+11**	**8.12E+01**	**2.39E-01**	**3.40E+02**	**51.1**
Rico-2 22617	**Rico Hot Springs**	**this study**	**37.70103**	**-108.03044**	**5.43**	**5.43**	**7.21E+11**	**1.49E+01**	**9.39E-02**	**1.58E+02**	**67.9**
Rico-3B 22617	**Rico Hot Springs**	**this study**	**37.70286**	**-108.02914**	**5.41**	**5.46**	**7.15E+11**	**7.08E-01**	**2.80E-02**	**2.53E+01**	**67.6**
Rico-3 22517 redo	**Rico Hot Springs**	**this study**	**37.70286**	**-108.02914**	**5.06**	**5.17**	**5.33E+11**	**4.26E+01**	**4.55E+00**	**9.36E+00**	**63.3**
Rico 1	**Rico Hot Springs**	**this study**	**37.70193**	**-108.03115**	**5.43**	**5.44**	**2.02E+10**	**5.68E+00**	**4.72E-02**	**1.20E+02**	**67.9**
Rico 2	**Rico Hot Springs**	**this study**	**37.70103**	**-108.03044**	**5.68**	**5.68**	**5.00E+09**	**2.20E+01**	**8.62E-02**	**2.55E+02**	**71.0**
Rico-01	Rico Hot Springs	Easley and Morgan, 2013	37.70193	-108.03115	5.88	5.88	n.a.	7.22E+04	1.44E+02	5.01E+02	73.5
Dunton-1 022617	**Dunton Hot Spring**	**this study**	**37.77279**	**-108.09319**	**2.52**	**3.11**	**6.52E+11**	**4.87E-01**	**5.89E-01**	**8.27E-01**	**31.5**
Dunton-2 22617	**Dunton Hot Spring**	**this study**	**37.77283**	**-108.09306**	**2.70**	**4.55**	**5.89E+11**	**6.96E-01**	**1.57E+00**	**4.43E-01**	**33.8**
Geyser Warm Spring	**Geyser Warm Spring**	**this study**	**37.74694**	**-108.11758**	**3.39**	**3.39**	**6.50E+09**	**2.84E+01**	**1.61E-01**	**1.76E+02**	**42.4**
Paradise Warm Spring 22617	**Paradise Warm Spring**	**this study**	**37.75419**	**-108.13190**	**2.33**	**2.72**	**7.21E+11**	**5.26E-01**	**5.12E-01**	**1.03E+00**	**29.1**
Lemon 22517	**Lemon Hot Spring**	**this study**	**38.01529**	**-108.05390**	**0.98**	**0.95**	**1.16E+11**	**4.66E+00**	**1.51E+01**	**3.08E-01**	**12.2**
Vapor Caves 022517	**Weisbaden Vapor Caves (Ouray)**	**this study**	**38.02306**	**-107.66827**	**0.85**	**0.81**	**3.87E+10**	**1.92E+01**	**2.02E+01**	**9.49E-01**	**10.6**
Orvis Hot Springs 22517	**Orvis Hot Springs**	**this study**	**38.13394**	**-107.73496**	**0.05**	**0.05**	**5.60E+11**	**4.01E+03**	**1.47E+00**	**2.73E+03**	**0.6**
LC06-CoOrv-1	Orvis Hot Springs	Karlstrom et al, 2013	38.13315	-107.73434	0.06	0.06	2.85E+09	n.a.	n.a.	n.a.	0.7
Pinkerton Hot Spring	Pinkerton Spring	this study	37.44929	-107.80475	0.93	0.87	3.52E+10	4.30E+00	1.82E+01	2.36E-01	11.6
LC06CO-BB-2	Pinkerton Spring	Karlstrom et al, 2013	37.44929	-107.80475	1.28	1.28	6.96E+12	n.a.	n.a.	n.a.	16.0
LC06-PgS-1	Pagosa Springs	Karlstrom et al, 2013	37.26453	-107.01083	0.08	0.08	1.81E+10	n.a.	n.a.	n.a.	1.0
LC06CO-WWG-1	Wagon Wheel Hot Springs	Karlstrom et al, 2013	37.74833	-106.83217	0.33	0.33	5.22E+11	n.a.	n.a.	n.a.	4.1
WWG-01	Wagon Wheel Hot Springs	Easley and Morgan, 2013	37.74833	-106.83217	0.23	0.23	n.a.	4.17E+05	1.66E+02	2.51E+03	2.9

Table 1. Results of gas analyses of San Juan springs from previous studies (Karlstrom et al, 2013; Easley and Morgan, 2013) and new samples (in bold type).

Significant mantle components were detected in our samples from the eastern and southern San Juan Mountains, but systematically lower than those from the WSJ Mountains. We measured value of 0.87 R_A at Pinkerton Hot Spring near Durango which is lower, but comparable to the previously measured value of 1.28 R_A at this site (Karlstrom et al, 2013). A similar value of 0.81 R_A was measured at Weisbaden Vapor Caves in Ouray. Finally, we measured a value of 0.05 R_A at Orvis Hot Spring north of Ouray. This value closely matches the previously measured value of 0.06Ra at this site (Karlstrom et al, 2013) and is also between our threshold values for detectable mantle signature (>0.1 R_A) and no significant mantle signature (<0.02 R_A).

Previous studies also measured a couple of San Juan springs that were not sampled for this study. Wagon Wheel Gap spring in the eastern San Juan Mountains near the Creede Caldera has relatively low mantle helium with R_A values ranging from 0.23-0.33 R_A (Karlstrom et al, 2013; Easley and Morgan, 2013). Pagosa Hot Spring in the southeastern San Juan Mountains falls in the same range as Orvis values, between detectable mantle signature and no mantle signature, with a R_A value of 0.08 R_A (Karlstrom et al, 2013).

Hydrochemistry

Stable isotopes

Results of oxygen isotope analyses of San Juan spring waters are reported in Table 2 and are shown in Figure 7 plotted relative to the Global Meteoric Water Line (GMWL). The main trend seen in these results is that the clear majority of samples plot directly along the GMWL. This indicates that the waters of most springs in this study are dominantly meteoric. However, there are a couple exceptions to this general trend. The samples from Geyser Warm Spring show slight depletion in ^{18}O compared to the GMWL, which could be interpreted to indicate subsurface boiling and steam condensation. In contrast, Paradise Warm Spring shows slight ^{18}O enrichment compared to the GMWL which could be interpreted as ^{18}O enrichment indicative of a component of deep

geothermal brines in the spring fluid. These brines are fluids which have spent a longer time at depth, and thereby at higher temperatures.

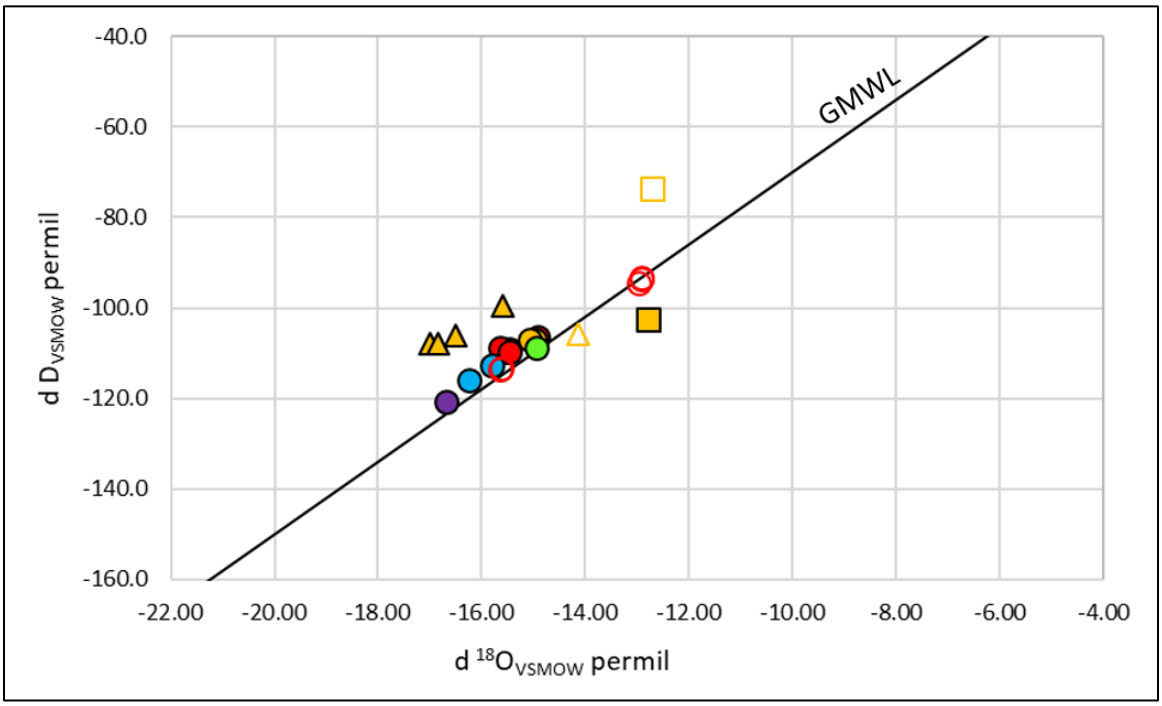

Figure 7. Deuterium vs Delta O-18 for San Juan geothermal springs plotted relative to the Global Meteoric Water Line (GMWL). Filled symbols represent new data from this study, whereas hollow symbols represent isotopic data from the literature (Easley and Morgan, 2013; Oerter, 2011) Only Paradise and Geyser Warm Spring samples exhibit slight deviation from the GMWL. Overall, WSJ Hot Springs plot along the GMWL, indicating that their fluids are dominantly meteoric by volume.

Sample Name	Rico1	Rico1a	Rico2	Rico3	Rico 1	Rico 2	Rico 3	Dunton 1	Dunton 2
Sample Date	11/13	11/13	11/13	11/13	2/26	2/26	2/25	2/25	2/25
Latitude	37.7019	37.7019	37.7010	37.7029	37.7019	37.7010	37.7029	37.7728	37.7728
Longitude	-108.0312	-108.0309	-108.0304	-108.0291	-108.0312	-108.0304	-108.0291	-108.0932	-108.0931
Temperature (degC)	n.a.	n.a.	n.a.	n.a.	42	43.9	42.4	36.3	35.3
pH	6.89	6.74	6.96	7.07	6.63	6.54	6.57	6.82	6.82
Conductivity (µS)	n.a.	n.a.	n.a.	n.a.	1510	1403	1570	1778	1777
TDS (mg/L)	3417	2841	3481	3735	3435	3189	3655	1760	1818
Ca (mg/L)	631	526	703	757	690	622	746	347	346
Mg (mg/L)	94.7	96.2	95.8	95.1	94.8	95.4	96.0	34.6	34.5
Na (mg/L)	65.8	67.8	70.1	76.5	66.4	62.9	74.8	33.4	33.3
K (mg/L)	27.4	28.2	27.5	27.7	27.0	27.4	27.9	19.7	19.6
HCO_3 (mg/L)	1690	1193	1551	1666	1458	1413	1564	914	912
Cl (mg/L)	1.6	4.3	3.6	3.5	4.7	4.3	4.1	5.4	5.6
SO_4 (mg/L)	906	926	1030	933	1040	924	1099	348	348
balance (%)	-4.2	-1.5	-0.3	2.9	0.1	-0.3	0.5	-0.5	-0.7
SiO_2 (mg/L)	114	112	120	125	114	107	118	33	33
F (mg/L)	2.4	2.1	2.4	2.0	2.2	2.3	2.0	1.1	1.1
NO2 (mg/L)	n.a.	n.a.	0.6	0.5	n.a.	n.a.	n.a.	n.a.	n.a.
Br (mg/L)	n.a.	n.a.	0.2	0.1	n.a.	n.a.	n.a.	n.a.	n.a.
NO3 (mg/l)	1.2	0.3	0.1	0.1	0.8	0.8	0.7	1.0	1.2
PO4 (mg/l)	n.a.	n.a.	n.a.	n.a.	1657	3595	1950	n.a.	n.a.
Al (mg/L)	0.03	0.03	0.03	0.02	0.01	0.01	0.00	0.03	0.02
As (mg/L)	0.06	0.04	0.06	0.04	0.07	0.06	0.05	0.04	0.04
B (mg/L)	0.08	0.08	0.08	0.08	0.08	0.08	0.08	0.07	0.07
Ba (mg/L)	0.03	0.02	0.03	0.02	0.01	0.01	0.01	0.02	0.02
Be (mg/L)	n.a.	n.a.	n.a.	n.a.	n.a.	n.a.	n.a.	n.a.	n.a.
Cd (mg/L)	n.a.	n.a.	n.a.	n.a.	n.a.	n.a.	n.a.	n.a.	n.a.
Co (mg/L)	n.a.	n.a.	n.a.	n.a.	n.a.	n.a.	n.a.	n.a.	n.a.
Cr (mg/L)	0.01	0.01	0.01	0.01	0.01	0.01	0.01	n.a.	n.a.
Cu (mg/L)	0.02	0.02	0.02	0.02	n.a.	n.a.	n.a.	n.a.	n.a.
Fe (mg/L)	5.7	0.2	5.6	4.7	6.0	5.5	4.8	n.a.	n.a.
Li (mg/L)	n.a.	n.a.	n.a.	n.a.	n.a.	n.a.	n.a.	n.a.	n.a.
Mn (mg/L)	1.0	0.5	1.2	1.4	1.1	0.9	1.3	1.4	1.4
Mo (mg/L)	n.a.	n.a.	n.a.	n.a.	n.a.	n.a.	n.a.	n.a.	n.a.
Ni (mg/L)	n.a.	n.a.	n.a.	n.a.	n.a.	n.a.	n.a.	n.a.	n.a.
Pb (mg/L)	0.04	0.05	0.04	0.04	0.04	0.03	0.04	0.03	0.03
Se (mg/L)	n.a.	n.a.	n.a.	n.a.	n.a.	n.a.	n.a.	n.a.	n.a.
Si (mg/L)	53.4	52.5	56.3	58.4	53.1	50.0	55.0	15.4	15.4
Sr (mg/L)	8.0	7.5	9.2	10.3	9.2	8.0	10.4	3.8	3.8
V (mg/L)	0.003	0.003	0.003	0.003	n.a.	n.a.	n.a.	n.a.	n.a.
Zn (mg/L)	0.09	0.10	0.04	0.02	0.04	0.09	0.03	0.00	0.00
U (mg/L)	0.009	n.a.	n.a.	n.a.	n.a.	n.a.	n.a.	n.a.	n.a.
$d^{18}O$	-15.6	-14.9	-15.6	-15.5	-15.5	-15.6	-15.5	-15.0	-15.1
dD	-109.1	-106.3	-109.2	-109.2	-109.7	-108.7	-109.7	-106.9	-107.0

Table 2) New hydrochemical analyses of San Juan Hot Springs

Sample Name	GWS A	GWS B	GWS C	Paradise Hot Spring	Lemon Hot Springs	Box Canyon (Ouray)	Wiesbaden Vapor Cave (Ouray)	Orvis Hot Spring
Sample Date	7/7	7/7	7/7	2/25	2/25	11/13	2/25	2/25
Latitude	37.7029	37.7029	37.7029	37.7542	38.0153	38.0196	38.0231	38.1339
Longitude	-108.0291	-108.0291	-108.0291	-108.1319	-108.0539	-107.6759	-107.6683	-107.7350
Temperature (degC)	27.0	27.0	27.0	42.7	23.2	n.a.	48.6	50.9
pH	6.29	6.29	6.29	6.42	7.99	8.3	6.71	6.58
Conductivity (µS)	2740	2740	2740	4880	1770	n.a.	1785	1999
TDS (mg/L)	1060	1050	1050	6756	3075	1737	1216	2271
Ca (mg/L)	176	174	173	173	124	371	338	290
Mg (mg/L)	33.0	32.7	32.7	22.5	9.6	8.2	7.7	15.8
Na (mg/L)	392.6	396.7	391.9	1947.2	737.7	117.0	122.1	429.7
K (mg/L)	29.6	29.7	37.1	326.9	78.7	10.2	10.8	28.2
HCO_3 (mg/L)	1695	1699	1710	698	880	129	173	406
Cl (mg/L)	2.6	2.6	2.7	3407.1	266.9	45.4	34.9	81.3
SO_4 (mg/L)	169	163	169	164	1049	1056	1057	1311
balance (%)	-3.4	-3.2	-3.8	-3.5	-3.2	-1.7	-5.6	-1.5
SiO_2 (mg/L)	42	42	40	150	95	48	52	41
F (mg/L)	n.a.	n.a.	n.a.	4.7	4.4	3.4	3.0	3.9
NO2 (mg/L)	2.3	1.2	1.3	3917.3	n.a.	0.8	n.a.	n.a.
Br (mg/L)	n.a.	1.2	1.0	6.4	1.7	0.3	0.7	1.0
NO3 (mg/l)	3.7	3.7	4.1	2.5	2.0	0.3	1.0	0.8
PO4 (mg/l)	n.a.	n.a.	n.a.	n.a.	1808	n.a.	2129	4942
Al (mg/L)	0.01	0.01	0.02	0.03	0.04	0.04	0.03	0.02
As (mg/L)	0.03	n.a.	0.02	0.08	0.17	0.04	0.43	0.03
B (mg/L)	0.13	0.12	0.12	10.48	2.76	0.22	1.11	0.19
Ba (mg/L)	0.40	0.40	0.39	0.26	n.a.	0.03	n.a.	n.a.
Be (mg/L)	n.a.	n.a.	n.a.	n.a.	n.a.	n.a.	n.a.	n.a.
Cd (mg/L)	n.a.	n.a.	n.a.	n.a.	n.a.	n.a.	n.a.	n.a.
Co (mg/L)	n.a.	n.a.	n.a.	n.a.	n.a.	n.a.	n.a.	n.a.
Cr (mg/L)	n.a.	n.a.	n.a.	n.a.	n.a.	n.a.	n.a.	n.a.
Cu (mg/L)	0.01	0.01	0.01	n.a.	n.a.	0.02	n.a.	n.a.
Fe (mg/L)	n.a.	n.a.	n.a.	0.2	0.1	n.a.	0.8	n.a.
Li (mg/L)	n.a.	n.a.	n.a.	10.7	4.3	n.a.	0.7	n.a.
Mn (mg/L)	0.6	0.6	0.6	0.6	0.1	0.8	0.1	0.9
Mo (mg/L)	n.a.	n.a.	n.a.	n.a.	n.a.	n.a.	n.a.	n.a.
Ni (mg/L)	n.a.	n.a.	n.a.	n.a.	n.a.	n.a.	n.a.	n.a.
Pb (mg/L)	n.a.	n.a.	n.a.	0.02	0.02	0.03	0.03	0.03
Se (mg/L)	n.a.	n.a.	n.a.	n.a.	n.a.	n.a.	n.a.	n.a.
Si (mg/L)	19.5	19.4	18.9	70.0	44.2	22.3	24.5	18.9
Sr (mg/L)	5.1	5.1	5.0	2.9	3.6	6.4	7.7	6.2
V (mg/L)	n.a.	n.a.	n.a.	n.a.	n.a.	n.a.	n.a.	n.a.
Zn (mg/L)	n.a.	n.a.	0.03	0.01	0.00	0.02	0.00	0.02
U (mg/L)	n.a.	n.a.	n.a.	n.a.	n.a.	n.a.	n.a.	n.a.
$d^{18}O$	-16.5	-17.0	-16.9	-12.8	-15.0	-15.8	-16.2	-16.7
dD	-106.0	-107.9	-107.9	-102.5	-108.8	-112.6	-115.8	-120.7

Table 2 cont.) New hydrochemical analyses of San Juan Hot Springs

Solutes and geothermal indicators

In addition to oxygen isotopes, concentrations of several common solutes were also analyzed (Table 2) to create a multiple-tracer approach to evaluating the potential impact of mixing, water-rock interactions, and geothermal brines on the chemistry of spring fluids. Concentrations of key "geothermal tracers" typically enriched in geothermal brines (lithium, fluoride, boron, and bromine vs chloride) were plotted for each spring. The results of this analysis are displayed in Figure 8. Paradise Warm Spring had by far the highest chlorine content of sampled springs with measured concentrations of >3000ppm. Moderate chloride values were measured at Lemon, Ouray, and Orvis springs, while Rico, Dunton, and Geyser had relatively low chlorine concentration. Fluorine enrichment was greatest at Paradise Warm Spring and Lemon Hot Spring, with some enrichment also observed in the Ouray and Orvis samples, and lowest at Rico, Dunton, and Geyser. Lithium concentrations were below method detection limits for many samples, yet a similar still emerges from the data. Paradise Warm Spring also has the most lithium enrichment (10.7ppm) of any measured Colorado spring. Lithium levels were also moderately enriched at Lemon, with progressively decreasing concentrations at Orvis, Ouray, and Rico. This trend persists for boron and bromine as well where greatest concentrations were measured at Paradise Warm Spring, second greatest measured at Lemon Hot Spring, moderate values measured at Ouray and Orvis, and lowest values measured at Rico, Dunton, and Geyser springs.

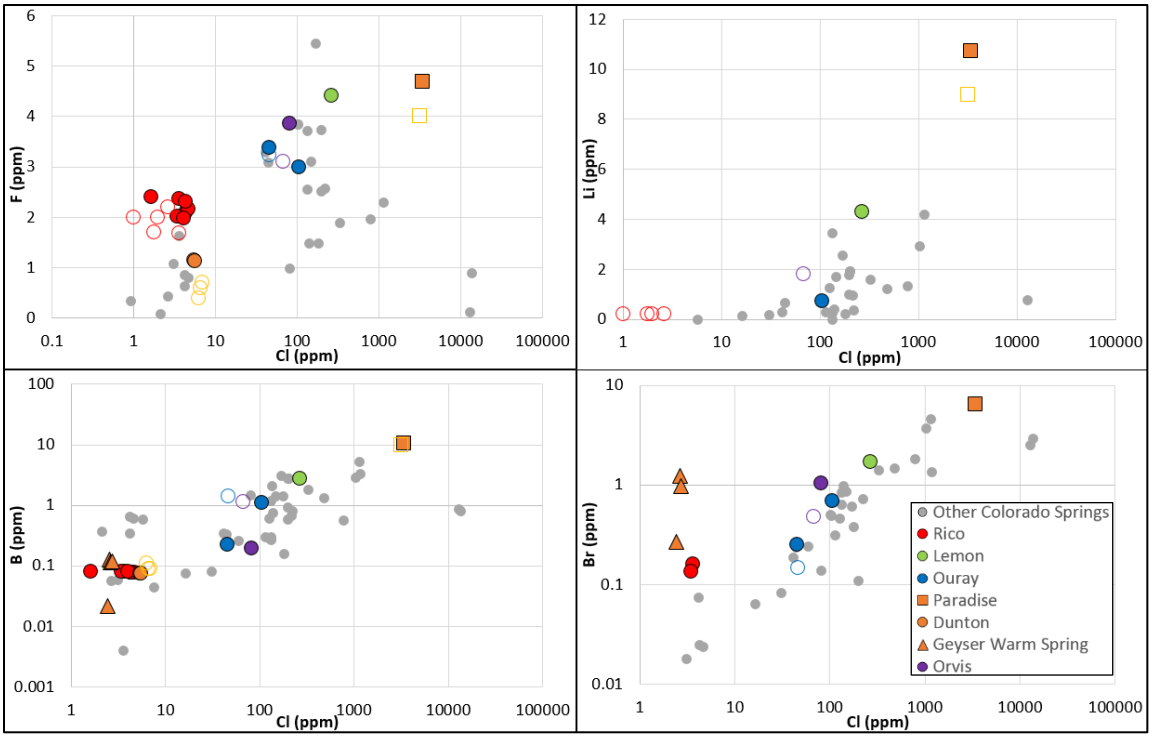

Figure 8. Geothermal indicators (fluorine, lithium, boron, and bromine) plotted relative to chlorine for WSJ springs where constituents were above method detection limits. Other Colorado springs are plotted as gray dots for broader reference of western U.S. geothermal systems. Filled symbols for WSJ samples indicate new data from this study, whereas hollow samples represent literature data from these same springs.

TDS and major cations/anions

The major cation and anion chemistry of WSJ springs, as well as TDS, are reported in Table 2 and summarized using a Piper diagram (Fig. 9). On the Piper diagram, every sample is plotted with size of the symbol scaled with TDS. Fluids at Rico are calcium-bicarbonate/sulfate waters with TDS values up to 3735ppm. Despite the geographic proximity of Dunton, Geyser, and Paradise springs (within 2mi), they all have very distinct hydrochemical signatures. Dunton is also calcium-bicarbonate water but with much lower TDS values than Rico, only up to 1818ppm. In contrast to Dunton, sodium and potassium are the primary cations at Geyser Warm Spring. However, Geyser Warm Spring also has bicarbonate-type anion chemistry and relatively low TDS (up to 1060ppm). Paradise Warm Springs has sodium/potassium-type anion chemistry similar to Geyser Warm Spring, but has a distinct chloride-type anion chemistry and extremely high TDS (6756ppm). Lemon Hot Spring is also sodium/potassium rich, but no dominant anion chemistry type. TDS is also relatively high at Lemon Hot Spring with measured

values up to 3075ppm. Ouray and Orvis both have bicarbonate-sulfate type hydrochemical signatures. Orvis, cation chemistry is less strongly dominated by bicarbonate than Ouray. Furthermore, Orvis has notably higher TDS (up to 2528ppm) than the springs in Ouray (up to 1737ppm). Overall these results show that, despite the very close proximity of some of the springs in this study, all of the springs have distinct hydrochemical signatures. These results, paired with our other analytical techniques will help us interpret the circulation pathways of these fluids that generate their distinct chemical signature.

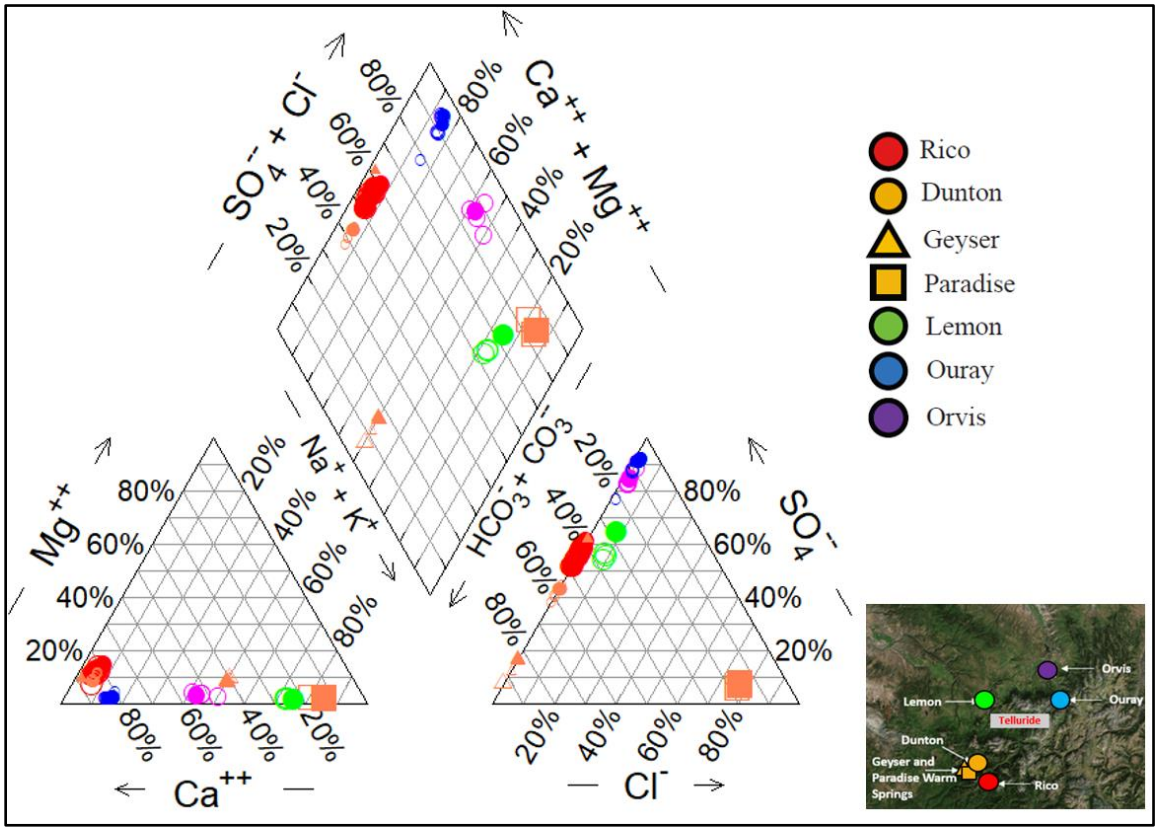

Figure 9. Major cation and anion analysis summarized using a Piper diagram. The bottom left ternary plot shows the proportions of major cations for each fluid, while the bottom right ternary plot show the same for major anions. Both of these ternary plots are then projected onto the central summary diamond. The bottom right map shows the geographic distribution of these springs. Symbol size is scaled so that samples with higher TDS have larger symbols. Finally, solid symbols are new data contributed by this study whereas hollow symbols are samples from previous studies (Karlstrom et al, 2013; Barrett and Pearl, 1978, Easley and Morgan, 2013).

Geothermometry estimates

Table 3 presents new geothermometry estimates for WSJ springs. Table 3 also includes geothermometry estimates of these same springs from compiled from several previous studies (Easley and Morgan, 2013; Karlstrom et al, 2013; Oerter, 2011; Smith et al, 2018). Several silica-based and cation-based geothermometers were applied to these samples. These analyses are tabulated in Table 3 and resulted in a wide range of reservoir temperature estimates for each spring (Rico: 22-157 º C, Dunton: 33-119 º C, Geyser Warm Spring: 42-112 º C, Paradise: 39-250 º C, Lemon: 14-198 º C). The discussion section below assesses which geothermometers are considered most reliable at each spring.

Sample Name	Sample Date	Data and Geothermometry Source	Temp (deg C)	Amorphous Silica	Alpha Cristobalite	Beta Cristobalite	Chalcedony conductive
Rico1	**Nov-16**	**This Study**	**n.a.**	**24**	**94**	**45**	**119**
Rico1a	**Nov-16**	**This Study**	**n.a.**	**23**	**93**	**44**	**118**
Rico2	**Nov-16**	**This Study**	**n.a.**	**27**	**97**	**48**	**122**
Rico3	**Nov-16**	**This Study**	**n.a.**	**29**	**100**	**50**	**125**
Rico 1	**Feb-17**	**This Study**	**42.0**	**23**	**94**	**45**	**119**
Rico 2	**Feb-17**	**This Study**	**43.9**	**20**	**90**	**42**	**115**
Rico 3	**Feb-17**	**This Study**	**42.4**	**25**	**96**	**47**	**121**
Rico-01	n.a.	Easley and Morgan, 2013	41.0	n.a.	n.a.	n.a.	128
Rico-02	n.a.	Easley and Morgan, 2013	44.0	n.a.	n.a.	n.a.	129
Rico #1	Jul-08	Oerter, 2011	40.8	n.a.	n.a.	n.a.	126 - 129
Rico #2	Jul-08	Oerter, 2011	42.8	n.a.	n.a.	n.a.	124 - 127
Rico #3	Jul-08	Oerter, 2011	41.1	n.a.	n.a.	n.a.	127 - 130
Rico: Diamond Drill Hole	Jan-76	Barrett and Pearl, 1978; Oerter, 2011	44.0	26	n.a.	n.a.	120 - 122
Rico: Big Geyser W.S.	Sep-75	Barrett and Pearl, 1978; Oerter, 2011	34.0	22	n.a.	n.a.	115 - 117
Rico: Big Geyser W.S.	Apr-76	Barrett and Pearl, 1978; Oerter, 2011	36.0	35	n.a.	n.a.	129 - 133
Rico: Geyser W.S.	Sep-75	Barrett and Pearl, 1978; Oerter, 2011	38.0	22	n.a.	n.a.	115 - 117
Rico: Little Spring	Sep-75	Barrett and Pearl, 1978; Oerter, 2011	38.0	26	n.a.	n.a.	120 - 122
Rico: Little Spring	Jan-76	Barrett and Pearl, 1978; Oerter, 2011	39.0	26	n.a.	n.a.	120 - 122
Dunton 1	**Feb-17**	**This Study**	**36.3**	**n.a.**	**33**	**n.a.**	**52**
Dunton 2	**Feb-17**	**This Study**	**35.3**	**n.a.**	**34**	**n.a.**	**52**
Dunton Hot Spring	Jul-08	Oerter, 2011	41.4	n.a.	n.a.	n.a.	59 - 61
Dunton Hot Spring	Sep-75	Barrett and Pearl, 1978; Oerter, 2011	44.0	n.a.	n.a.	n.a.	54 - 56
Dunton Hot Spring	Jan-76	Barrett and Pearl, 1978; Oerter, 2011	42.0	n.a.	n.a.	n.a.	51 - 53
Dunton Hot Spring	Apr-76	Barrett and Pearl, 1978; Oerter, 2011	42.0	n.a.	n.a.	n.a.	52 - 55
GWS A	**Jul-17**	**This Study**		**n.a.**	**43**	**n.a.**	**63**
GWS B	**Jul-17**	**This Study**		**n.a.**	**43**	**n.a.**	**63**
GWS C	**Jul-17**	**This Study**		**n.a.**	**42**	**n.a.**	**61**
Geyser Warm Spring	Jul-08	Oerter, 2011	28.5	n.a.	n.a.	n.a.	64 - 66
Geyser Warm Spring	Sep-75	Barrett and Pearl, 1978; Oerter, 2011; Smith et al, 2018	28.0	n.a.	n.a.	n.a.	57 - 60
Paradise Hot Spring	**Feb-17**	**This Study**	**42.7**	**39**	**111**	**61**	**137**
Paradise Hot Spring	Jul-08	Oerter, 2011	43.4	n.a.	n.a.	n.a.	142 - 146
Paradise Hot Spring	Sep-75	Barrett and Pearl, 1978; Oerter, 2011; Smith et al, 2018	46.0	39	n.a.	n.a.	134 - 137
Paradise Hot Spring	Jan-76	Barrett and Pearl, 1978; Oerter, 2011; Smith et al, 2018	40.0	56	n.a.	n.a.	153 - 159
Paradise Hot Spring	Apr-76	Barrett and Pearl, 1978; Oerter, 2011; Smith et al, 2018	42.0	39	n.a.	n.a.	134 - 137
Lemon Hot Springs	**Feb-17**	**This Study**	**23.2**	**14**	**83**	**35**	**107**
Lemon Hot Springs	Sep-75	Barrett and Pearl, 1978	31.0	15	n.a.	n.a.	n.a.
Lemon Hot Springs	Jan-76	Barrett and Pearl, 1978	33.0	17	n.a.	n.a.	n.a.
Lemon Hot Springs	Apr-76	Barrett and Pearl, 1978	33.0	14	n.a.	n.a.	n.a.

Table 3) Compilation of geothermometry estimates for WSJ springs from this project and several previous studies (Easley and Morgan, 2013; Karlstrom et al, 2013; Oerter, 2011; Smith et al, 2018; Barrett and Pearl, 1978)

Sample Name	Sample Date	Data and Geothermometry Source	Quartz conductive	Quartz adiabatic	Na-K-Ca	Na-K-Ca Mg correction	K/Mg Giggenbach 1986
Rico1	**Nov-16**	**This Study**	**145**	**139**	**54**	**54**	**65**
Rico1a	**Nov-16**	**This Study**	**144**	**138**	**58**	**58**	**65**
Rico2	**Nov-16**	**This Study**	**148**	**142**	**52**	**52**	**65**
Rico3	**Nov-16**	**This Study**	**150**	**143**	**52**	**52**	**65**
Rico 1	**Feb-17**	**This Study**	**145**	**139**	**52**	**52**	**64**
Rico 2	**Feb-17**	**This Study**	**141**	**136**	**54**	**54**	**65**
Rico 3	**Feb-17**	**This Study**	**147**	**141**	**52**	**52**	**65**
Rico-01	n.a.	Easley and Morgan, 2013	153	n.a.	48	48	n.a.
Rico-02	n.a.	Easley and Morgan, 2013	154	n.a.	44	44	n.a.
Rico #1	Jul-08	Oerter, 2011	137 - 154	n.a.	48	n.a.	61
Rico #2	Jul-08	Oerter, 2011	135 - 152	n.a.	50	n.a.	61
Rico #3	Jul-08	Oerter, 2011	138 - 155	n.a.	55	n.a.	64
Rico: Diamond Drill Hole	Jan-76	Barrett and Pearl, 1978; Oerter, 2011	132 - 148	n.a.	56	n.a.	66
Rico: Big Geyser W.S.	Sep-75	Barrett and Pearl, 1978; Oerter, 2011	127 - 143	n.a.	57	n.a.	65
Rico: Big Geyser W.S.	Apr-76	Barrett and Pearl, 1978; Oerter, 2011	140 - 157	n.a.	56	n.a.	67
Rico: Geyser W.S.	Sep-75	Barrett and Pearl, 1978; Oerter, 2011	127 - 143	n.a.	59	n.a.	66
Rico: Little Spring	Sep-75	Barrett and Pearl, 1978; Oerter, 2011	132 - 148	n.a.	58	n.a.	30
Rico: Little Spring	Jan-76	Barrett and Pearl, 1978; Oerter, 2011	132 - 148	n.a.	16	n.a.	67
Dunton 1	**Feb-17**	**This Study**	**84**	**86**	**49**	**49**	**69**
Dunton 2	**Feb-17**	**This Study**	**84**	**87**	**49**	**49**	**69**
Dunton Hot Spring	Jul-08	Oerter, 2011	76 - 92	n.a.	48	n.a.	63
Dunton Hot Spring	Sep-75	Barrett and Pearl, 1978; Oerter, 2011	70 - 88	n.a.	50	n.a.	64
Dunton Hot Spring	Jan-76	Barrett and Pearl, 1978; Oerter, 2011	68 - 85	n.a.	47	n.a.	66
Dunton Hot Spring	Apr-76	Barrett and Pearl, 1978; Oerter, 2011	71 -87	n.a.	52	n.a.	66
GWS A	**Jul-17**	**This Study**	**94**	**95**	**103**	**80**	**79**
GWS B	**Jul-17**	**This Study**	**94**	**95**	**104**	**80**	**79**
GWS C	**Jul-17**	**This Study**	**93**	**94**	**112**	**79**	**85**
Geyser Warm Spring	Jul-08	Oerter, 2011	81 - 96	n.a.	100	n.a.	73
Geyser Warm Spring	Sep-75	Barrett and Pearl, 1978; Oerter, 2011; Smith et al, 2018	74 - 91	n.a.	103	60	75
Paradise Hot Spring	**Feb-17**	**This Study**	**161**	**153**	**240**	**167**	**156**
Paradise Hot Spring	Jul-08	Oerter, 2011	151 - 169	n.a.	n.a.	n.a.	154
Paradise Hot Spring	Sep-75	Barrett and Pearl, 1978; Oerter, 2011; Smith et al, 2018	144 - 162	n.a.	252	202	154
Paradise Hot Spring	Jan-76	Barrett and Pearl, 1978; Oerter, 2011; Smith et al, 2018	161 - 181	n.a.	248	178	154
Paradise Hot Spring	Apr-76	Barrett and Pearl, 1978; Oerter, 2011; Smith et al, 2018	144 - 162	n.a.	250	190	155
Lemon Hot Springs	**Feb-17**	**This Study**	**134**	**130**	**195**	**151**	**123**
Lemon Hot Springs	Sep-75	Barrett and Pearl, 1978	n.a.	n.a.	198	n.a.	n.a.
Lemon Hot Springs	Jan-76	Barrett and Pearl, 1978	n.a.	n.a.	192	n.a.	n.a.
Lemon Hot Springs	Apr-76	Barrett and Pearl, 1978	n.a.	n.a.	195	n.a.	n.a.

Table 3 cont.) Compilation of geothermometry estimates for WSJ springs from this project and several previous studies (Easley and Morgan, 2013; Karlstrom et al, 2013; Oerter, 2011; Smith et al, 2018; Barrett and Pearl, 1978.

CO_2 flux transects

Table 4 summarizes the background measurements taken at the Rico field site. Atmospheric CO_2 concentrations ranged between 210-242 ppm. To constrain the potential impact of daily biogenic CO_2 flux cycles caused by plant respiration, we took measurements at three vegetated points within the field site in the morning, afternoon, and evening. The maximum change in flux rate between these different times of day for each point allows us to establish how much flux rate may change over the course of the day due to biogenic cycles. The results showed that biogenic flux cycles have a minor influence at Rico, with the maximum change in linear flux rate over the course of a day being 0.18g/m^2/hr.

Time	Latitude	Longitude	Concentration (ppm CO_2)	Change in Concentration (ppm CO_2)	Change in Time (s)	Linear Flux Rate (g/m^2/hr)	Quadratic Flux Rate (g/m^2/hr)	Type
9:00 AM	37.70179	-108.03120	359	145	120	0.88	0.99	Vegetated Soil
9:00 AM	37.70173	-108.03117	350	42	120	0.27	0.33	Vegetated Soil
9:00 AM	37.70171	-108.03122	417	116	120	0.71	0.89	Vegetated Soil
9:00 AM	37.70171	-108.03122	220	18	120	-0.08	1.05	Air
3:00 PM	37.70179	-108.03120	343	119	120	0.7	0.79	Vegetated Soil
3:00 PM	37.70173	-108.03117	249	32	120	0.17	0.19	Vegetated Soil
3:00 PM	37.70171	-108.03122	341	124	120	0.72	0.87	Vegetated Soil
3:00 PM	37.70171	-108.03122	210	0	120	0.01	-0.01	Air
6:00 PM	37.70179	-108.03120	312	118	120	0.7	0.8	Vegetated Soil
6:00 PM	37.70173	-108.03117	264	33	120	0.19	0.33	Vegetated Soil
6:00 PM	37.70171	-108.03122	380	102	120	0.61	0.68	Vegetated Soil
6:00 PM	37.70171	-108.03122	242	-11	120	0.02	-0.47	Air

Table 4) Background CO_2 flux measurements at the Rico field site for establishing atmospheric CO_2 and the magnitude of daily biogenic CO_2 flux cycles

Figure 10 shows the results of plotting measured CO_2 flux values (Table 5) into transects at the Rico Hot Springs in context of the previously mapped/inferred locations of local structures. These results reveal a wide range of CO_2 linear flux rate values at

Rico from 0 to 36.32g/m^2/hr. The high end of this range is quite dramatic, being comparable to High Point Source Flux values measured near large carbonic springs like Soda Dam in the Valles Caldera (Smith, 2016). For our analysis, we consider any linear flux rate >1.60g/m^2/hr to be representative of detectable endogenic CO_2 degassing. Using this constraint, we see several patterns emerge from the data relating to the regional structural features. Elevated linear flux rates were measured on both the eastern and western transects as they crossed the inferred location of the Last Chance fault. On the other hand, no significant elevation in linear flux rate was detected on either transect as they crossed the inferred location of the Nellie Bly fault. Peak linear flux rates values were measured in a cluster between the Nellie Bly and Last Chance faults, south of the three hot springs, and only on the eastern transect. These spatial trends allow us to refine the location of these inferred faults and make interpretations about the near-surface volatile pathways at Rico in the "Discussion" section below.

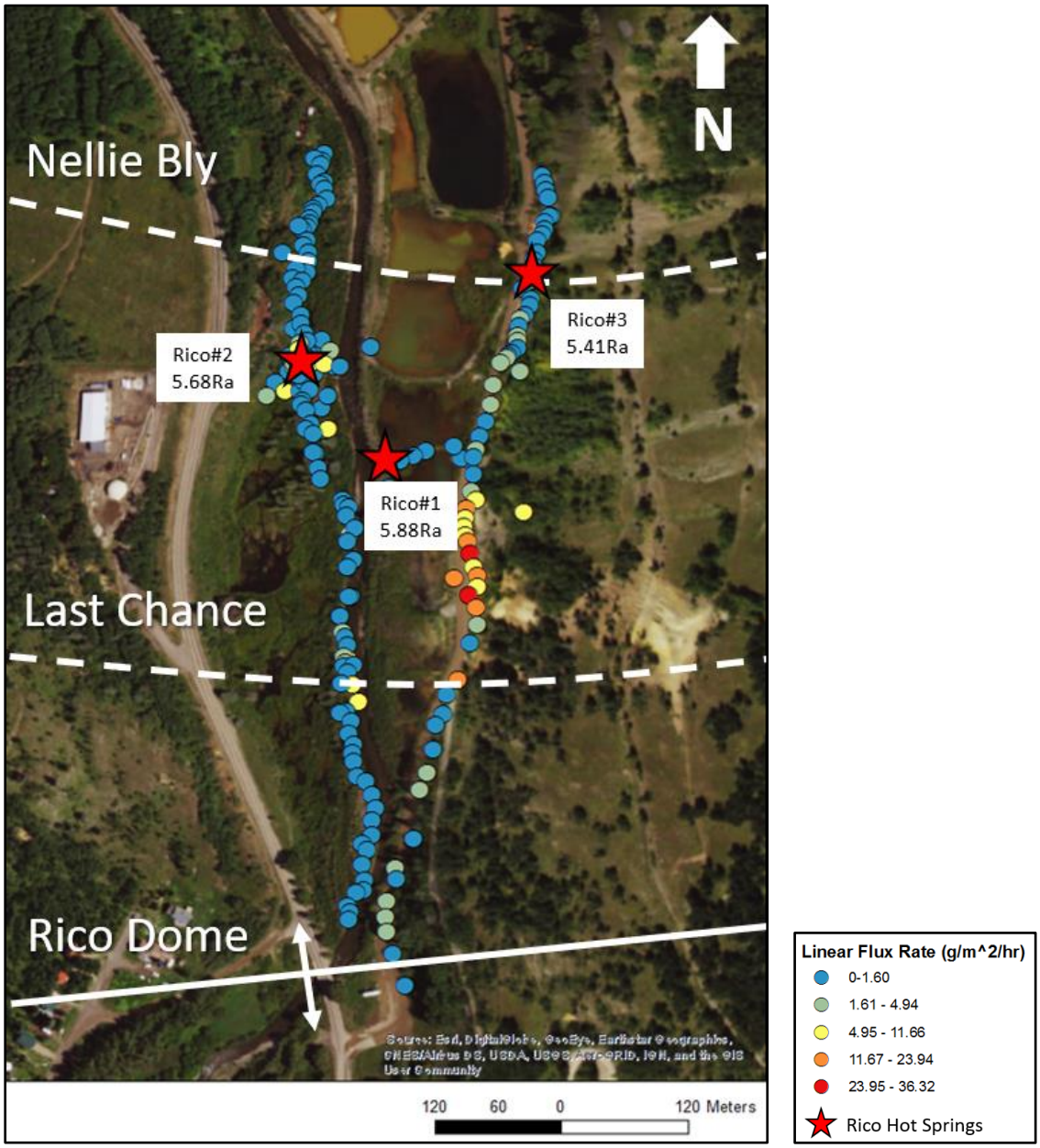

Figure 10. Results of the CO_2 flux transects at the Rico Hot Springs (red stars). Locations of the Rico Dome, Last Chance Fault, and Nellie Bly Fault are adapted from Pratt et al, 1969. The previously inferred locations of the Last Chance fault appears to be accurate based on elevated flux values across this location on both transects, indicating the presence of a planar feature with high permeability. However, elevated flux is not similarly observed on either transect across the previously inferred trace of the Nellie Bly Fault. Furthermore, the area of maximum flux values only occurs on the eastern transect and therefore isn't fully explained by just these E-W trending structures.

Sample Name	Date	Latitude	Longitude	Concentration (ppm CO_2)	Change in Concentration (ppm CO_2)	Change in Time (s)	Linear Flux Rate ($g/m^2/hr$)	Quadratic Flux Rate ($g/m^2/hr$)
RHS12	7/21/2016	37.70195	-108.03131	1108	13	120	-0.61	-0.46
RHS31	7/21/2016	37.70219	-108.03121	477	19	120	0.13	0.15
RHS27	7/21/2016	37.70145	-108.03101	548	22	120	0.03	0.04
RHS6	7/21/2016	37.70184	-108.03132	454	38	120	0.78	0.94
RHS16	7/21/2016	37.70188	-108.03093	480	42	120	0.21	0.3
RHS13	7/21/2016	37.70201	-108.03115	493	55	120	0.29	0.31
RHS20	7/21/2016	37.70201	-108.03062	547	83	120	0.27	0.34
RHS8	7/21/2016	37.70177	-108.03143	572	97	120	0.69	0.61
RHS32	7/21/2016	37.70213	-108.03127	524	99	120	0.54	0.66
RHS26	7/21/2016	37.70160	-108.03104	551	117	120	0.67	0.67
RHS14	7/21/2016	37.70202	-108.03108	554	126	120	0.52	0.73
RHS23	7/21/2016	37.70183	-108.03110	576	153	120	0.88	1
RHS15	7/21/2016	37.70206	-108.03104	587	156	120	0.92	1.02
RHS30	7/21/2016	37.70206	-108.03117	646	188	120	1.12	1.7
RHS4	7/21/2016	37.70186	-108.03125	648	202	120	1.19	1.82
RHS25	7/21/2016	37.70168	-108.03098	679	212	120	1.24	1.53
RHS33	7/21/2016	37.70264	-108.03137	685	249	120	1.36	1.65
RHS19	7/21/2016	37.70198	-108.03096	748	294	120	2.16	3.03
RHS5	7/21/2016	37.70188	-108.03127	839	336	120	1.84	2.04
RHS9	7/21/2016	37.70168	-108.03150	1219	456	120	2.8	0.45
RHS3	7/21/2016	37.70190	-108.03127	3272	603	120	3.45	6.47
RHS29	7/21/2016	37.70191	-108.03110	1762	902	120	5.65	7.41
RHS18	7/21/2016	37.70189	-108.03101	1525	1000	100	6.83	8.56
RHS21	7/21/2016	37.70171	-108.03135	1534	1001	99	6.65	8.29
RHS28	7/21/2016	37.70146	-108.03098	1678	1008	108	7.1	8.41
RHS2	7/21/2016	37.70191	-108.03121	5221	1073	1	0	0
RHS17	7/21/2016	37.70188	-108.03088	28574	1531	2	0	0
RHS10	7/21/2016	37.70197	-108.03115	7360	2354	1	0	0
RHS11	7/21/2016	37.70193	-108.03116	6673	2636	2	0	0
RHS34	7/21/2016	37.70106	-108.03046	101474	3562	1	0	0
Rico-1	11/14/2016	37.70125	-108.02979	n.a.	175	120	0.46	0.48
Rico-2	11/14/2016	37.70126	-108.02985	n.a.	127	120	0.76	0.84
Rico-3	11/14/2016	37.70134	-108.02991	n.a.	21	120	0.19	0.12
Rico-4	11/14/2016	37.70131	-108.03015	n.a.	73	120	0.42	0.52
Rico-5	11/14/2016	37.70128	-108.03026	n.a.	54	120	0.32	0.38
Rico-6	11/14/2016	37.70124	-108.03037	n.a.	30	120	0.2	0.24
RHS300	9/2/2017	37.70316	-108.02917	417	-17	120	0.05	0.05
RHS301	9/2/2017	37.70311	-108.02914	235	55	120	0.34	0.41
RHS302	9/2/2017	37.70306	-108.02913	242	26	120	0.16	0.16
RHS303	9/2/2017	37.70301	-108.02911	235	67	120	0.41	0.42
RHS304	9/2/2017	37.70289	-108.02908	246	30	120	0.18	0.2
RHS305	9/2/2017	37.70289	-108.02910	6345	1810	1	0	0
RHS306	9/2/2017	37.70285	-108.02914	4084	1338	4	0	0
RHS307	9/2/2017	37.70280	-108.02914	327	113	120	0.69	0.81
RHS308	9/2/2017	37.70276	-108.02917	288	76	120	0.49	0.52
RHS309	9/2/2017	37.70272	-108.02921	454	231	120	1.45	1.59
RHS310	9/2/2017	37.70264	-108.02921	342	120	120	0.75	0.81
RHS311	9/2/2017	37.70264	-108.02921	410	185	120	1.14	1.23
RHS312	9/2/2017	37.70259	-108.02924	290	76	120	0.47	0.52
RHS313	9/2/2017	37.70255	-108.02924	456	224	120	1.34	1.69
RHS314	9/2/2017	37.70250	-108.02923	405	100	120	0.6	0.71
RHS315	9/2/2017	37.70249	-108.02926	281	67	120	0.41	0.47
RHS316	9/2/2017	37.70245	-108.02926	793	513	120	2.69	3.75

Table 5) CO_2 flux measurements taken near the Rico Hot Springs

Sample Name	Date	Latitude	Longitude	Concentration (ppm CO_2)	Change in Concentration (ppm CO_2)	Change in Time (s)	Linear Flux Rate ($g/m^2/hr$)	Quadratic Flux Rate ($g/m^2/hr$)
RHS317	9/2/2017	37.70245	-108.02927	694	437	120	2.52	3.27
RHS318	9/2/2017	37.70240	-108.02933	585	225	120	0.55	0.58
RHS319	9/2/2017	37.70233	-108.02926	443	218	120	1.3	1.54
RHS320	9/2/2017	37.70229	-108.02927	423	209	120	1.27	1.47
RHS321	9/2/2017	37.70222	-108.02931	610	309	120	1.08	1.25
RHS322	9/2/2017	37.70220	-108.02935	730	493	120	2.83	3.55
RHS323	9/2/2017	37.70215	-108.02936	439	152	120	0.87	1.04
RHS324	9/2/2017	37.70208	-108.02937	623	310	120	1.74	2.2
RHS325	9/2/2017	37.70205	-108.02937	896	622	120	3.7	4.5
RHS326	9/2/2017	37.70200	-108.02937	456	195	120	1.15	1.27
RHS327	9/2/2017	37.70197	-108.02943	334	78	120	0.46	0.49
RHS328	9/2/2017	37.70195	-108.02946	407	166	120	1	1.07
RHS329	9/2/2017	37.70193	-108.02947	1326	865	120	4.7	5.63
RHS330	9/2/2017	37.70190	-108.02952	140	660	120	3.77	4.31
RHS331	9/2/2017	37.70184	-108.02935	816	449	120	2.57	2.98
RHS332	9/2/2017	37.70175	-108.02958	772	458	120	2.63	3.11
RHS333	9/2/2017	37.70162	-108.02960	713	323	120	1.74	1.96
RHS334	9/2/2017	37.70151	-108.02964	443	202	120	1.23	1.31
RHS335	9/2/2017	37.70141	-108.02969	372	131	120	0.8	0.87
RHS336	9/2/2017	37.70132	-108.02973	665	435	120	2.63	2.91
RHS337	9/2/2017	37.70127	-108.02975	347	130	120	0.74	0.87
RHS338	9/2/2017	37.70115	-108.02975	413	177	120	0.98	1.15
RHS339	9/2/2017	37.70104	-108.02977	798	552	120	3.3	3.42
RHS340	9/2/2017	37.70098	-108.02973	1276	918	120	5.46	5.78
RHS341	9/2/2017	37.70092	-108.02981	1775	1002	53	15.1	12
RHS342	9/2/2017	37.70090	-108.02932	1434	101	71	10.33	9.86
RHS343	9/2/2017	37.70086	-108.02982	1200	906	120	5.54	6.08
RHS344	9/2/2017	37.70080	-108.02983	1338	1006	59	11.66	12.24
RHS345	9/2/2017	37.70074	-108.02982	1358	1012	63	11.46	11.06
RHS346	9/2/2017	37.70070	-108.02980	1676	1016		19.86	17.41
RHS347	9/2/2017	37.70062	-108.02978	1977	1053	23	36.32	34.73
RHS348	9/2/2017	37.70053	-108.02975	1353	1001	93	7.58	7.97
RHS349	9/2/2017	37.70047	-108.02972	1373	1019	33	23.94	22.26
RHS350	9/2/2017	37.70040	-108.02972	1338	1012	76	9.41	9.71
RHS351	9/2/2017	37.70034	-108.02979	1421	1022	25	31.59	29.62
RHS352	9/2/2017	37.70045	-108.02991	1621	1010	37	18.85	18.07
RHS353	9/2/2017	37.70026	-108.02973	1425	1001	43	16.98	16.05
RHS354	9/2/2017	37.00230	-108.02974	1474	1014	31	21.5	21.17
RHS355	9/2/2017	37.70014	-108.02972	997	717	120	4.09	4.57
RHS356	9/2/2017	37.70002	-108.02978	433	162	120	0.94	0.98
RHS357	9/2/2017	37.69977	-108.02988	1301	1015	51	15.04	15.69
RHS358	9/2/2017	37.69967	-108.02998	449	213	120	1.26	1.45
RHS359	9/2/2017	37.69954	-108.03001	461	237	120	1.43	1.77
RHS360	9/2/2017	37.69947	-108.03007	500	249	120	1.49	1.86
RHS361	9/2/2017	37.69930	-108.03009	441	143	120	0.74	0.88
RHS362	9/2/2017	37.69915	-108.03014	551	307	120	1.79	2.09
RHS363	9/2/2017	37.69903	-108.03020	399	178	120	1.7	1.7
RHS364	9/2/2017	37.69870	-108.03026	478	238	120	1.49	1.5
RHS365	9/2/2017	37.69851	-108.03041	596	360	120	2.09	3.68
RHS366	9/2/2017	37.69843	-108.03040	364	152	120	0.92	0.94
RHS367	9/2/2017	37.69828	-108.03048	686	415	120	2.39	2.75
RHS368	9/2/2017	37.69818	-108.03049	674	447	120	2.53	3.04
RHS369	9/2/2017	37.69808	-108.03048	664	401	120	2.34	2.51

Table 5 cont.) CO_2 flux measurements taken near the Rico Hot Springs

Sample Name	Date	Latitude	Longitude	Concentration (ppm CO_2)	Change in Concentration (ppm CO_2)	Change in Time (s)	Linear Flux Rate ($g/m^2/hr$)	Quadratic Flux Rate ($g/m^2/hr$)
RHS370	9/2/2017	37.69793	-108.03043	343	110	120	0.7	0.66
RHS371	9/2/2017	37.69772	-108.03033	412	174	120	1.1	1.23
500	10/27/2017	37.70179	-108.03120	359	145	120	0.88	0.99
501	10/27/2017	37.70173	-108.03117	350	42	120	0.27	0.33
502	10/27/2017	37.70171	-108.03122	417	116	120	0.71	0.89
504	10/27/2017	37.70331	-108.03101	262	62	120	0.39	0.49
505	10/27/2017	37.70326	-108.03104	254	46	120	0.27	0.33
506	10/27/2017	37.70327	-108.03110	252	51	120	0.34	0.38
507	10/27/2017	37.70323	-108.03105	270	37	120	0.24	0.26
508	10/27/2017	37.70317	-108.03108	319	47	120	0.34	0.37
509	10/27/2017	37.70312	-108.03101	308	93	120	0.55	0.6
510	10/27/2017	37.70310	-108.03105	299	46	120	0.33	0.31
511	10/27/2017	37.70307	-108.03101	267	58	120	0.36	0.39
512	10/27/2017	37.70300	-108.03099	249	45	120	0.28	0.33
513	10/27/2017	37.70296	-108.03107	235	36	120	0.21	0.26
514	10/27/2017	37.70294	-108.03111	256	27	120	0.18	0.19
515	10/27/2017	37.70291	-108.03111	270	44	120	0.3	0.27
516	10/27/2017	37.70287	-108.03114	264	68	120	0.42	0.51
517	10/27/2017	37.70284	-108.03114	257	62	120	0.35	0.44
518	10/27/2017	37.70281	-108.03116	340	120	120	0.71	0.84
519	10/27/2017	37.70280	-108.03120	375	80	120	0.52	0.57
520	10/27/2017	37.70282	-108.03123	323	118	120	0.69	0.8
521	10/27/2017	37.70272	-108.03116	296	98	120	0.58	0.64
522	10/27/2017	37.70269	-108.03119	313	78	120	0.48	0.51
523	10/27/2017	37.70264	-108.03115	311	93	120	0.55	0.52
524	10/27/2017	37.70258	-108.03115	322	111	120	0.68	0.77
525	10/27/2017	37.70251	-108.03116	444	240	120	1.36	1.55
526	10/27/2017	37.70253	-108.03125	269	66	120	0.42	0.41
527	10/27/2017	37.70247	-108.03128	285	77	120	0.45	0.51
528	10/27/2017	37.70245	-108.03120	350	142	120	0.83	0.96
529	10/27/2017	37.70241	-108.03125	381	158	120	0.93	0.99
530	10/27/2017	37.70235	-108.03123	396	176	120	1.03	1.22
531	10/27/2017	37.70230	-108.03127	527	257	120	1.5	1.87
532	10/27/2017	37.70222	-108.03121	358	151	120	0.87	1.03
533	10/27/2017	37.70216	-108.03121	237	34	120	0.2	0.24
534	10/27/2017	37.70210	-108.03118	393	143	120	0.87	1.03
535	10/27/2017	37.70205	-108.03116	374	170	120	1	1.12
536	10/27/2017	37.70203	-108.03122	507	304	120	1.84	1.92
537	10/27/2017	37.70197	-108.03121	841	608	120	3.73	3.76
538	10/27/2017	37.70199	-108.03123	1035	832	120	5.27	5.83
539	10/27/2017	37.70193	-108.03119	1373	1010	98	7.89	7.82
540	10/27/2017	37.70191	-108.03119	1311	1007	103	7.39	8.63
541	10/27/2017	37.70192	-108.03124	1304	979	120	6.1	6.29
542	10/27/2017	37.70187	-108.03123	801	418	120	2.56	2.58
543	10/27/2017	37.70182	-108.03118	651	437	120	2.63	2.96
544	10/27/2017	37.70178	-108.03119	383	172	120	1.06	1.17
545	10/27/2017	37.70182	-108.03123	420	155	120	0.89	1.05
546	10/27/2017	37.70172	-108.03114	515	70	120	0.45	0.49
551	10/27/2017	37.70165	-108.03120	304	92	120	0.57	0.61
552	10/27/2017	37.70162	-108.03121	285	75	120	0.46	0.47
553	10/27/2017	37.70158	-108.03117	313	98	120	0.61	0.69
554	10/27/2017	37.70149	-108.03113	319	109	120	0.66	0.77
555	10/27/2017	37.70146	-108.03117	490	261	120	1.6	2.07

Table 5 cont.) CO_2 flux measurements taken near the Rico Hot Springs

Sample Name	Date	Latitude	Longitude	Concentration (ppm CO_2)	Change in Concentration (ppm CO_2)	Change in Time (s)	Linear Flux Rate ($g/m^2/hr$)	Quadratic Flux Rate ($g/m^2/hr$)
556	10/27/2017	37.70142	-108.03111	276	64	120	0.39	0.37
557	10/27/2017	37.70129	-108.03109	347	71	120	0.5	0.51
558	10/27/2017	37.70130	-108.03111	301	89	120	0.59	0.62
559	10/27/2017	37.70119	-108.03107	319	82	120	0.43	0.47
560	10/27/2017	37.70112	-108.03105	330	120	120	0.28	0.33
561	10/27/2017	37.70100	108.03107	299	85	120	0.5	0.58
562	10/27/2017	37.70098	-108.03086	484	259	120	1.57	1.75
563	10/27/2017	37.70095	-108.03085	317	100	120	0.62	0.84
564	10/27/2017	37.70093	-108.03081	355	113	120	0.72	0.78
565	10/27/2017	37.70087	-108.03083	325	99	120	0.64	0.79
566	10/27/2017	37.70075	-108.03080	780	491	120	2.87	4.69
567	10/27/2017	37.70079	-108.03075	229	17	120	0.1	0.1
568	10/27/2017	37.70070	-108.03082	298	76	120	0.48	0.54
569	10/27/2017	37.70058	-108.03076	294	57	120	0.37	0.39
570	10/27/2017	37.70053	-108.03082	318	70	120	0.41	0.42
571	10/27/2017	37.70033	-108.03079	269	32	120	0.2	0.18
572	10/27/2017	37.70033	-108.03081	320	102	120	0.62	0.71
573	10/27/2017	37.70020	-108.03088	230	19	120	0.11	0.05
574	10/27/2017	37.70009	-108.03086	510	288	120	1.84	2
575	10/27/2017	37.70006	-108.03084	332	109	120	0.7	0.73
576	10/27/2017	37.70000	-108.03082	317	92	120	0.55	0.58
577	10/27/2017	37.69991	-108.03082	1268	991	120	6.01	7.38
578	10/27/2017	37.69993	-108.03085	1058	761	120	4.94	5.78
579	10/27/2017	37.69989	-108.03084	599	359	120	2.22	2.47
580	10/27/2017	37.69986	-108.03085	344	93	120	0.59	0.62
585	10/27/2017	37.69987	-108.03076	336	92	120	0.56	0.77
586	10/27/2017	37.69982	-108.03082	284	44	120	0.27	0.29
587	10/27/2017	37.69974	-108.03078	1322	1009	81	9.41	9.65
588	10/27/2017	37.69975	-108.03087	312	70	170	0.43	0.49
589	10/27/2017	37.69962	-108.03072	1406	1007	108	6.94	6.94
590	10/27/2017	37.69956	-108.03083	377	127	120	0.8	0.82
591	10/27/2017	37.69955	-108.03088	249	14	120	0.08	0.07
592	10/27/2017	37.69949	-108.03079	242	14	120	0.04	0.09
593	10/27/2017	37.69941	-108.03081	256	16	120	0.11	0.11
594	10/27/2017	37.69934	-108.03077	308	36	120	0.23	0.23
595	10/27/2017	37.69928	-108.03078	246	23	120	0.14	0.15
596	10/27/2017	37.69922	-108.03077	268	35	120	0.21	0.22
597	10/27/2017	37.69912	-108.03073	245	17	120	0.11	0.14
598	10/27/2017	37.69909	-108.03066	368	-9	120	0.01	0
599	10/27/2017	37.69900	-108.03061	253	32	120	0.2	0.22
600	10/27/2017	37.69891	-108.03058	337	74	120	0.45	0.45
601	10/27/2017	37.69883	-108.03061	242	20	120	0.13	0.12
602	10/27/2017	37.69873	-108.03061	234	9	120	0.08	0.06
603	10/27/2017	37.69867	-108.03069	246	17	120	0.11	0.12
604	10/27/2017	37.69863	-108.03065	290	24	120	0.27	0.29
605	10/27/2017	37.69853	-108.03069	240	20	120	0.12	0.15
606	10/27/2017	37.69842	-108.03067	247	16	120	0.11	0.1
607	10/27/2017	37.69836	-108.03068	298	75	120	0.46	0.44
608	10/27/2017	37.69834	-108.03074	245	26	120	0.15	0.17
609	10/27/2017	37.69825	-108.03082	262	29	120	0.18	0.17
610	10/27/2017	37.69821	-108.03080	288	18	120	0.21	0.21
611	10/27/2017	37.69816	-108.03081	273	38	120	0.24	0.25

Table 5 cont.) CO_2 flux measurements taken near the Rico Hot Spring

Discussion

Mixing between Gas Sources for Helium Isotope Samples

During gas sampling for helium isotopes, it is possible to contaminate the sample with atmospheric gas if either the metal clamps do not completely seal the copper tube sample apparatus or if the copper tube was not thoroughly flushed with sample gas before sealing it shut. Furthermore, air can get into the groundwater and mix with fluids as they travel from the reservoir, resulting in air-saturated water (ASW). Due to this, highest R_A values from a spring are considered to be the most significant measurements, as long as any air or ASW contamination is corrected. Using other noble gases (Ne) it is possible to assess the degree of atmospheric contamination and make corrections to the measured R_A values.

For this gas mixing analysis, we establish mixing lines between ASW, mantle, and crustal gas. Ratios of key tracer gases are the axes of these mixing lines and are defined as:

$$R/R_A = \frac{(^3He/_{^4He})_{measured}}{(^3He/_{^4He})_{air}}$$

$$X = \frac{(He/Ne)_{measured}}{(He/Ne)_{air}}$$

Endmember values are defined as $R/R_A = 0.985R_A$ for ASW ratio, $= 0.02R_A$ for pure crustal helium ratio, and $= 8R_A$ for MORB values. The X value of ASW is 0.233, and for air it is 0.2882 (Hilton, 1995). There is virtually no neon in the mantle or crust, so the X values for these endmembers are defined by the measurable limit of the mass spectrometer (He/Ne= ~5000) (Whyte, personal communication). Figure 11 plots our gas samples along curves that are defined by mixing between these endmembers. The further a sample plots from the atmospheric endmember, the less it was contaminated by air and the greater confidence we have that our resultant R/R_A value is an accurate representation of crustal vs mantle gas components in that spring. The R/R_A value of samples can be

corrected for any air contamination to yield R_C/R_A values (reported in Table 1) using the equation (Craig et al, 1978):

$$\frac{R_C}{R_A} = \frac{\left(\frac{R_m}{R_A} * X\right) - 1}{X - 1}$$

Figure 11 shows that our samples from Rico Hot Springs and Geyser Warm Springs plot near the 50-75% mantle gas component endmembers, which gives us high confidence of low atmospheric contamination or ASW mixing for these samples. Samples from Dunton Hot Springs and Paradise Warm Spring are both somewhat shifted toward the ASW endmember. However, since they have high mantle signatures despite this component of contamination/mixing, we have high confidence that their actual mantle signatures in a non-contaminated sample would be at least, if not more so, dramatic. The least contaminated samples in this study were both Orvis and Wagon Wheel Gap Springs, which proves that their relatively low mantle signatures are accurate and not the results of sampling errors or fluid mixing. Lemon Hot Spring, Wiesbaden Spring in Ouray, and Pinkerton Hot Spring all show significant air contamination. All three of these samples yielded relatively low, but still detectable mantle gas signatures. However, due to this apparent contamination, it is likely that their true mantle gas ratio is greater than our measured results. Based on this result, we can be confident that all three of these springs do have a component of mantle gas but can't be confident in how high that mantle gas component may be. Therefore, these three springs would be candidates for resampling in future studies.

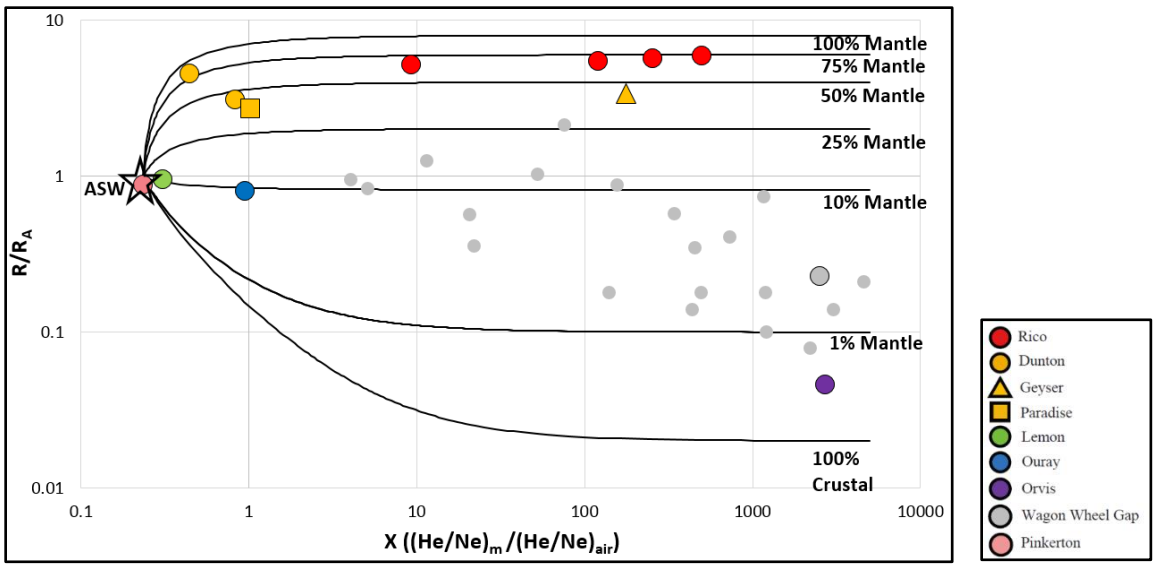

Figure 11. X vs R/R_A plot to determine atmospheric contamination as well as mixing between crustal and mantle gas endmembers for WSJ spring gas samples (outlined points) (this study; Karlstrom et. al, 2013) as well as other geothermal springs in Colorado (gray dots) (Karlstrom et al, 2013).

Correlations between regional mantle helium signature with magmatism and mantle tomography

To better understand the origin of the mantle derived helium, Figures 12 and 13 plot $^{3}He/^{4}He$ values on mantle tomographic maps and compare the results to a similar plot from Karlstrom et al. (2013). Figure 12A and 13A show relative mantle velocity structure at 125 km depths, assumed to be convecting (young) asthenosphere, and Figures 12B and 13B show similar plots for 60 km depths where Precambrian mantle lithosphere may still be preserved (Karlstrom et al., 2012). Both are from Schmandt and Humphrey (2010).

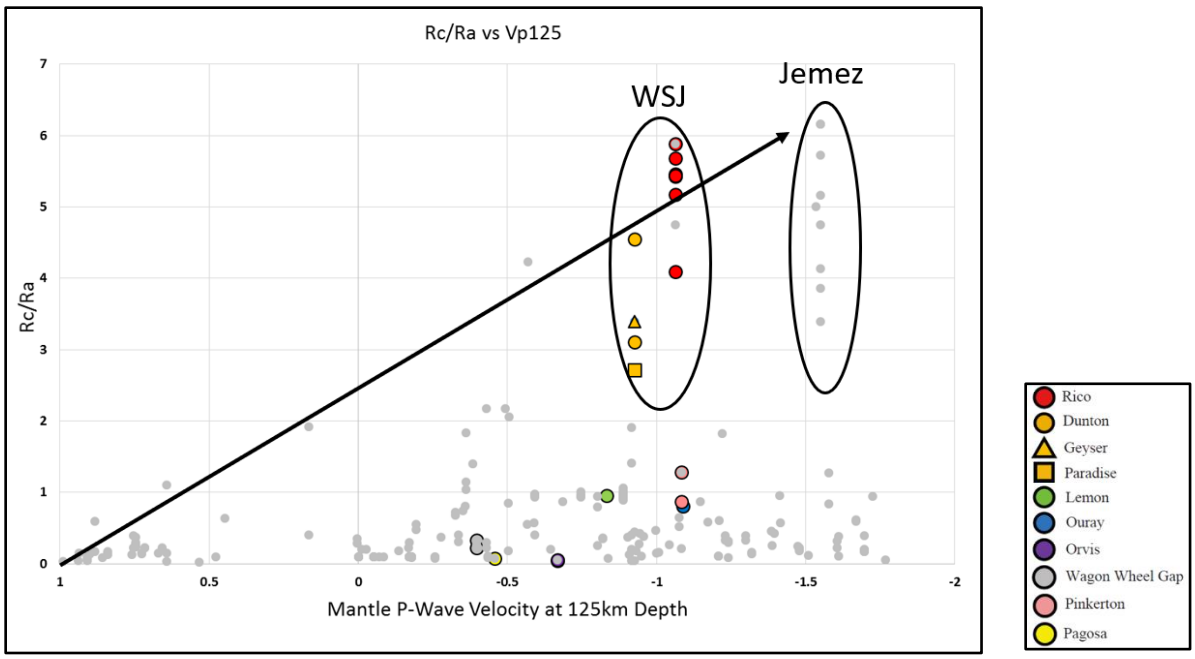

Figure 12A. Wedge plot of asthenospheric P-Wave velocity at 125km depth (Schmandt and Humphreys, 2010) versus mantle helium signature as Rc/Ra. Colored symbols are representative of San Juan Hot Spring samples from this study, whereas gray dots are helium isotope data from Karlstrom et al, 2013.

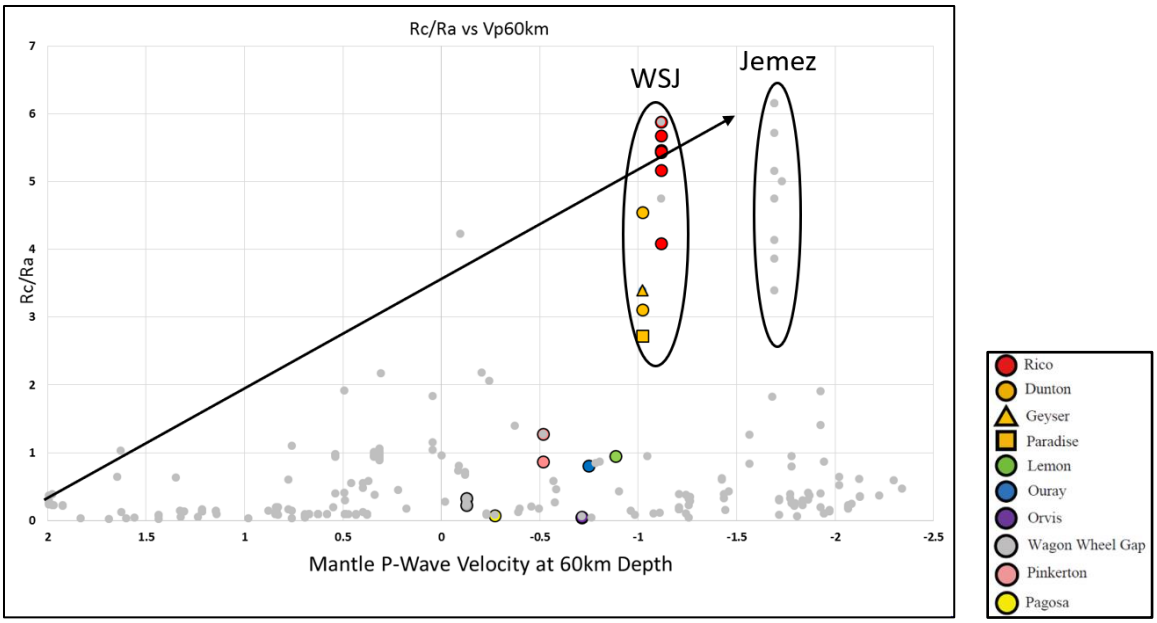

Figure 12B. Wedge plot of lithospheric P-Wave velocity at 60km depth (Schmandt and Humphreys, 2010) versus mantle helium signature as R_C/R_A. Colored symbols are representative of San Juan Hot Spring samples from this study, whereas gray dots are helium isotope data from Karlstrom et al, 2013.

For both depths, the spread of WSJ springs matches the existing trend from Karlstrom et al. (2013) of highest mantle helium overlying regions of lowest mantle

velocity. Furthermore, for both figures, we observe that the WSJ values are comparable to those from the Jemez/Valles volcanic system. This underscores the importance of proximity to low mantle velocity domains as a control on surface mantle helium expression. Figures 13A and 13B show the locations of young (<7Ma) magmatism (Gonzales, 2017) plotted on P-wave velocity maps at both 125km (Fig. 13A) and 60km (Fig. 13B) (Schmandt and Humphreys, 2010). Both show the association of low velocity mantle, young magmatism, and high $^{3}He/^{4}He$ values. This demonstrates how volatiles sourced in the asthenosphere are transported subvertically through the lithosphere and are then finally expressed as elevated $^{3}He/^{4}He$ ratios at carbonic springs.

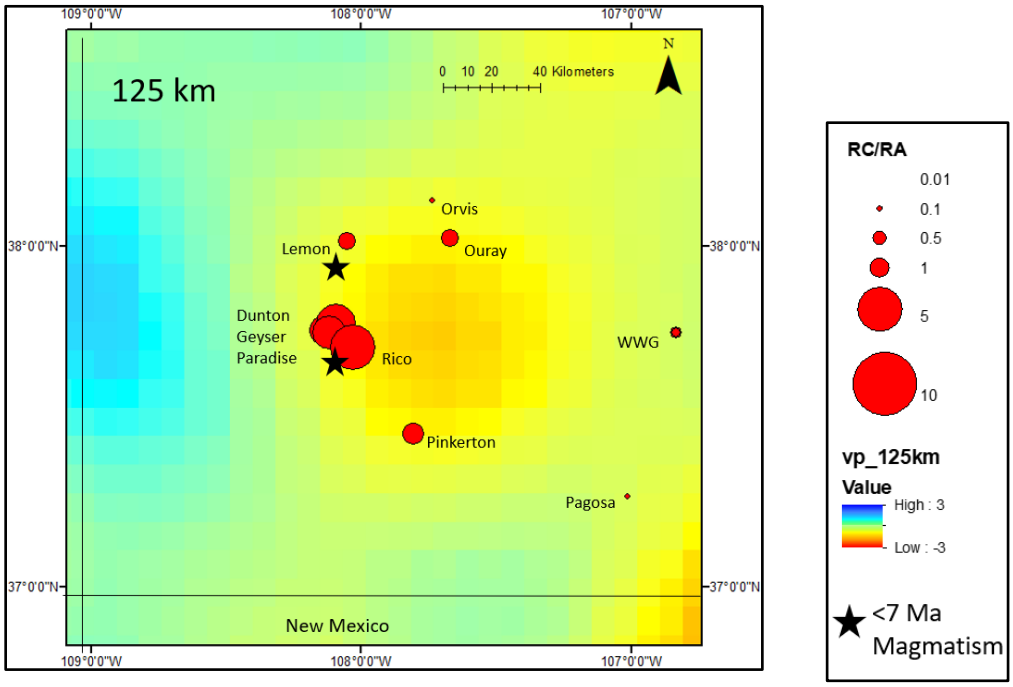

Figure 13A. Helium isotope ratios displayed over asthenospheric P-wave velocity at 125 km depth (Schmandt and Humphreys, 2010). Zone of lowest mantle tomography is centered under the study area, showing that mantle volatiles are likely sourced from asthenospheric degassing.

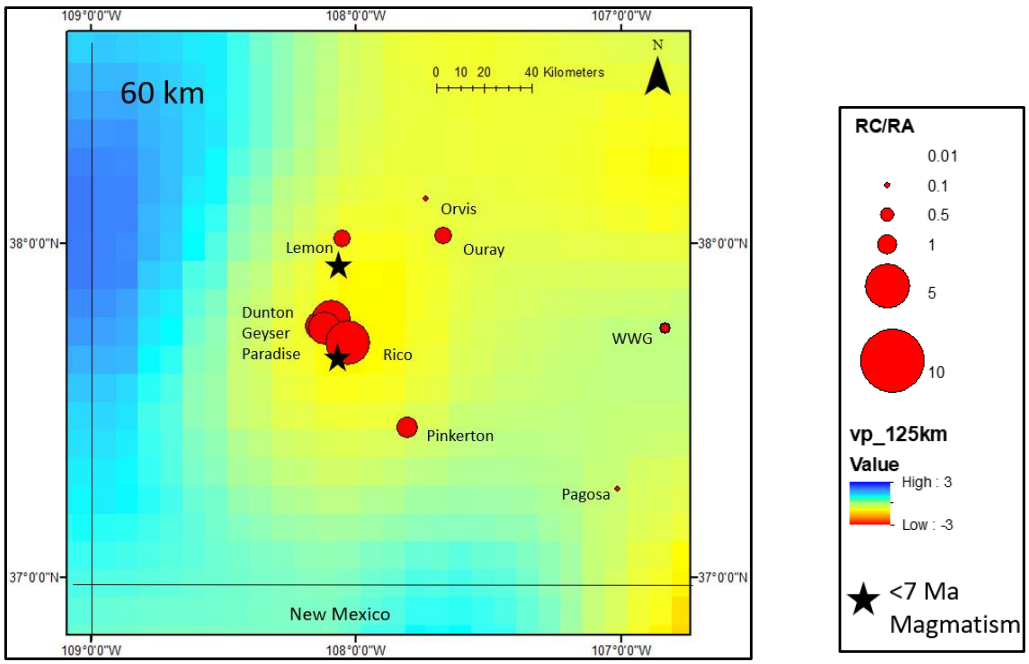

Figure 13B. Helium isotope ratios displayed over P-wave velocity at 60 km depth (Schmandt and Humphreys, 2010). Zone of lowest mantle tomography is generally centered under WSJ springs with highest mantle gas signature.

Fluid Circulation Pathways

We expand upon our understanding of the San Juan geothermal system by assessing major cation/anion enrichment and water "type" of each spring. In this way, we can make interpretations about circulation pathways, fluid residence times, and potential mixing between springs.

In addition to their low levels of geothermal brine indicators, the geothermal systems at Rico and Dunton springs share calcium-bicarbonate chemistry (Fig. 9). There are also two notable distinctions between Rico and Dunton hydrochemistry as both strontium and magnesium are elevated in Rico waters. Strontium is often enriched in basement rocks and thus Rico fluids are likely strontium-enriched due to increased interaction with regional basement rocks along the Rico Dome uplift (Fig. 4). Magnesium is commonly enriched due to water-rock interaction with alteration minerals such as illite or chlorite (Nicholson, 1993). Illite and chlorite are both present in alteration assemblages

of the Tertiary hornblende latite porphyry around Rico (Larson et al, 1994b). Therefore, Rico fluids likely picked up these elements during fluid-rock interaction at depth.

While Geyser and Paradise Springs are both located along the West Fork of the Dolores River less than 2 miles downstream of Dunton Springs, they both exhibit water chemistries distinct from Dunton and each other. Geyser cations are dominantly sodium and potassium with bicarbonate as the dominate anion type (Figure 9). The bicarbonate chemistry of this spring is also indicative of deep CO_2 rich gas condensing into subsurface water. Compared to Dunton and Paradise, Geyser is the only one not to emerge at river level, but instead ~1000ft above the river. Longer travel time from the reservoir may explain the lower temperatures and elevated bicarbonate at Geyser Warm Spring as these fluids have more time to cool as well as interact with limestone units in the Cutler Formation, Hermosa Formation, and Leadville Limestone at depth.

Several lines of evidence point to Paradise spring having the most significant thermal fluid component of springs in this study. Waters at Paradise spring are characterized by sodium/potassium – chloride type chemistry (Figure 9). As previously mentioned, chloride is very enriched in this spring with a concentration >3000mg/kg Cl; much higher than other springs in the study area which, except Lemon, are all below 10mg/kg Cl. Paradise also exhibits dramatic lithium enrichment (10mg/kg) with the highest concentration of lithium of all measured springs in Colorado. These constituents, paired with elevated levels of bromine, fluoride, silica are likely representative of a larger component of deep thermal fluids in this spring. Furthermore, this signature is often representative of fluids interacting with silicic to intermediate igneous rocks, such as the regional Tertiary monazite or latitie, at depth (White et al, 1984).

After Paradise Spring, Lemon Spring fluids show the greatest thermal fluids component of WSJ springs in this study. Lemon's cations are also sodium-potassium dominated but have no dominant anion chemistry. Fluorine, chlorine, and bromine are also elevated at Lemon compared to most WSJ springs, but still lower than Paradise. However, there isn't enrichment of ^{18}O in Lemon waters compared to the GMWL. Overall, this indicates that Lemon likely has a larger thermal fluid component than all WSJ except for Paradise, but that is component is still minor compared to meteoric

waters. Lithium levels are elevated at Lemon, but still notably lower than Paradise. Lithium concentrations are higher in fluids that interact with silicic or intermediate igneous rocks at depth, compared to fluids that interact with basaltic rocks (Nicholson, 1993). Lemon fluids likely derive residual heat from and follow pathways associated with the 600ka Specie Mesa basalt at depth, which may explain this relative reduction in lithium when compared to Paradise spring.

The Piper diagram shows that springs in the WSJ Mountains all have distinct geochemical signatures derived from different flow-paths and associated water-rock interactions. This trend is particularly apparent for the springs along the West Fork of the Dolores River as they all have very different chemistries despite spatial proximity. This demonstrates that there is limited mixing of fluids between springs which further indicates isolated circulation pathways and short fluid residence times.

Source of Spring Fluids in the Western San Juans

Using stable isotopes and geothermal tracers, we can assess the relative geothermal and meteoric components of spring fluids throughout the study area. In this way we can look at relationships between the gas and fluid circulation systems as well as potential connectivity between regional springs. As previously mentioned in the results, Figure 7 shows that the majority of spring oxygen isotope samples plot directly along the global meteoric water line (GMWL) indicating that most samples are dominantly meteoric fluids. This trend is bolstered by similar results observed in the geothermal solute data. Figure 8 displays that most sampled springs are low in key geothermal solutes such as chloride, lithium, boron, and fluoride. The key exceptions to this pattern Paradise Warm Spring and, to lesser extent, Lemon Warm Spring which display some enrichment of geothermal indicators. These two springs have a volumetrically minor, but geochemically potent, component of deep brine fluids. Brine fluids with longer residence times at higher temperature and in contact with bedrock leads to more accumulation of salts and trace elements from water-rock interactions. The low concentration of these solutes, paired with isotopic results along the GWML, in our samples overall indicates

that these spring fluids had short residence times at depth and minor mixing with deep geothermal brines (Shevenell et al, 1987).

Application of Geothermometers

All geothermometers are based on the fundamental assumption of equilibrium between reservoir fluids and components of the host rock. This further implies the assumption that constituents are present in a great enough quantity and that fluids stay in the reservoir long enough to achieve equilibrium (Fournier, 1974). For both the cation-based and silicon-based geothermometers we can geochemically assess the equilibrium state of our fluids, constrain these inherent uncertainties, and make more robust geothermometry estimates.

The cation-based geothermometers used in this study are Na-K-Ca (Fournier, 1977), Na-K-Ca with a Mg correction (Fournier and Potter, 1979), and K/Mg (Giggenbach, 1988). Water heated at depth will undergo exchange reactions with the local host rock. All these mentioned cation geothermometers utilize the abundance of feldspar and carbonate minerals to assess the equilibrium state of fluids with respect the dominant cations of these minerals. The Na-K-Ca geothermometer was generated to account for the common presence of carbonate minerals which was a factor left out of the previous Na-K geothermometer. The magnesium correction was added later on to account for waters that have elevated magnesium due to interactions with mica and chlorite-rich host rocks (Fournier and Potter, 1979; Smith et al, 2018). However, there are critical limitations to these geothermometers. Fournier states that this geothermometer is most appropriate for cooler source fluids <100 degrees C (Fournier, 1977) and that it is less effective when carbonates precipitate out of the geothermal fluids as they travel (Fournier,1973). Furthermore, cation geothermometers generally give less accurate estimates when reservoir fluids significantly mix with surface waters (Easley and Morgan, 2013). Both of these criterion for Na-K-Ca are not met by the majority of study springs. Travertine deposition was observed at every WSJ spring analyzed for geothermometry in this study except for Paradise Warm Spring. The stable isotope plot also shows that these same travertine-depositing springs have a great degree of mixing

with surface waters, with Paradise as somewhat of an exception (Figure 7). Yet, these Na-K-Ca geothermometers are also inappropriate at Paradise since it's source fluids are likely over >100 degrees (Oerter, 2011). Despite this, there is still a cation geothermometer that may be applied to Paradise. The K-Mg Giggenbach geothermometer assesses the cation equilibrium state resulting from water interaction with feldspars and micas. Paradise has limited surface water mixing compared to other study springs and its fluids achieve partial equilibrium with respect to the Na-K-Mg system (Figure 14) (Giggenbach, 1988; Oerter, 2011, Powelll and Cumming, 2010). Therefore, the K-Mg geothermometer may give a reasonable estimate at Paradise but should be supplemented with silica geothermometers.

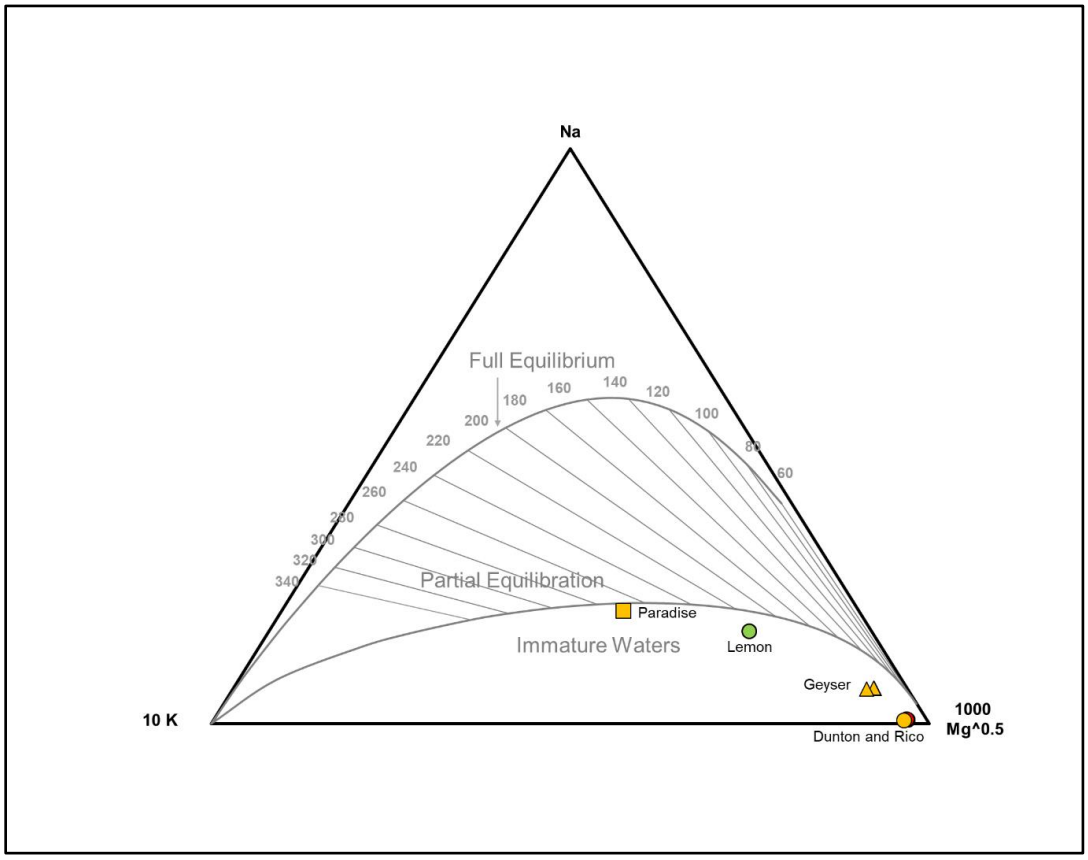

Figure 14. Giggenbach geoindicator showing degree of equilibrium of WSJ spring fluids from this study with respect to the Na-K-Mg system (Giggenbach, 1988; Powell and Cumming, 2010). Paradise spring plots along the margin of partial equilibrium, whereas the other samples are not in equilibrium with this system. Rico and Dunton are overlapping.

Silica geothermometers have several qualities which make them particularly valuable for estimating reservoir temperatures. First, they rely on fluid equilibrium with quartz which is abundant like feldspars, micas, and carbonates, but less reactive (Fournier, 1977; Smith et al, 2018). Therefore, these geothermometers are less skewed by mixing with surface waters, like we observe in the majority of our samples (Easley and Morgan, 2013). Silica geothermometers use solubility reactions to make reservoir temperature estimates. Quartz has multiple phases and so the appropriate silica geothermometer is chosen based on the equilibrium state of sample fluids with respect to these phases. The Log (K^2/Mg) vs SiO_2 plot (Figure 15) displays these silicia phase equilibrium states (Powell and Cumming, 2010).

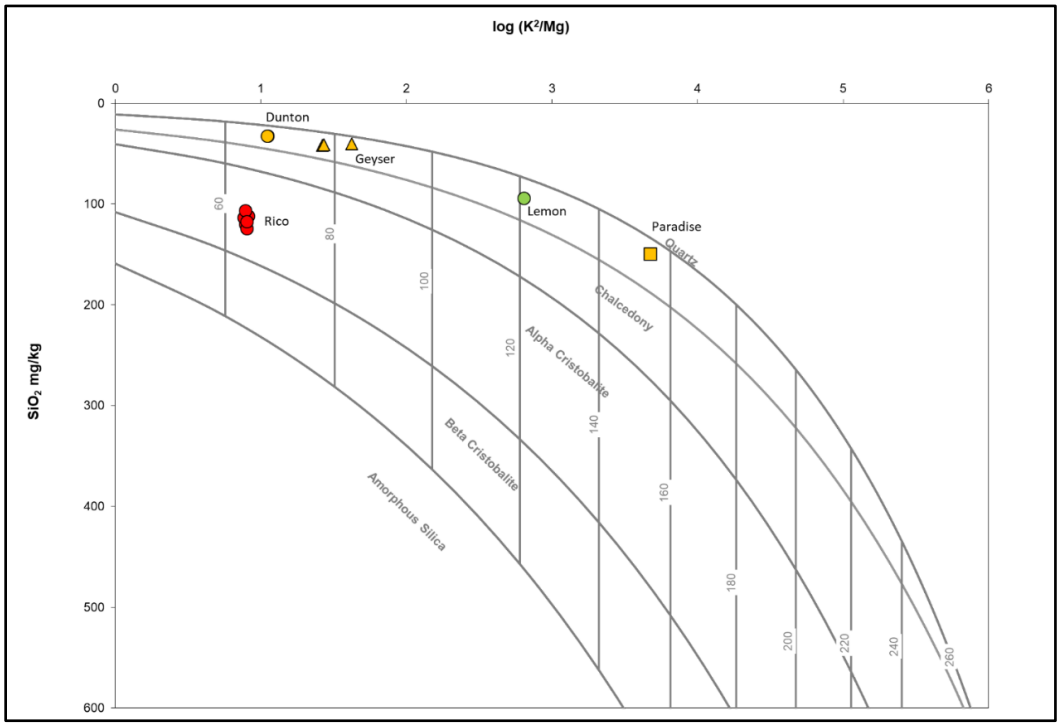

Figure 15. Log (K^2/Mg) vs SiO_2 plot showing equilibrium state of WSJ spring fluids with respect to quartz phases (Powell and Cumming, 2010). The majority of samples plot between the quartz and chalcedony equilibrium curves, whereas the Rico samples plot between alpha and beta cristobolite.

Geothermometry estimates by spring

Rico

Previous studies report varied geothermometry estimates at Rico based on several cation and silica geothermometers. However, Figure 15 shows that Rico fluids plot

between the equilibrium states for alpha and beta cristabolite. Alpha and beta cristabolite geothermometry estimates were generated using the Powell and Cumming, 2010 spreadsheet and are displayed in Table 3. Alpha cristabolite estimates range from 90-100 degrees, while beta cristabolite ranges from 42-50 degrees. These beta cristabolite estimates are similar to surface water temperatures, which is unrealistic especially considering the extensive mixing of Rico spring fluids with surface waters as they travel from the reservoir to the surface. Therefore, the alpha cristabolite estimates are likely closer to actual reservoir temperatures. Similar reservoir temperatures were also estimated recently by an MT survey at Rico (Dunnington, 2018). Combing these finding, our best estimate of reservoir temperatures at Rico is ~80-100 degC.

Dunton

Figure 15 shows Dunton samples plotting between the equilibrium states for quartz and chalcedony. Oerter, 2011 uses saturation indices as another way to elucidate which phase is closer to equilibrium. However, this study also presents mixed conclusions on whether quartz or chalcedony is the dominant phase. Using both of these phases, our best estimate is the range ~50-90degC which is similar to ranges proposed in previous studies (Oerter, 2011; Smith et al, 2018).

Geyser Warm Spring

Similar to Dunton, Geyser Warm Spring plots between quartz and chalcedony equilibrium phases (Figure 15) and Oerter, 2011 also has mixed results as to which phase is closer to equilibrium. Our estimate range from both these phases is ~60-95degC. This similar, yet slightly hotter, estimate compared to Dunton seems plausible due to their proximal locations and similar geochemistry.

Paradise Warm Spring

Paradise fluids plot between quartz and chalcedony equilibria but are somewhat closer to the quartz endmember (Figure 15). Quartz, chalcedony, and K/Mg geothermometers are all appropriate to use for these fluids and show strong agreement. Collectively, these give us a range of ~140-180degC reservoir temperature estimates,

which further agrees with previous studies (Oerter, 2011) as well as our measurements of increased geothermal indicators in these fluids.

Lemon Hot Spring

Lemon Hot Spring plots between quartz and chalcedony equilibrium like many of the above samples (Figure 15). Using both geothermometers, this gives us a range of ~110-130degC. This result is limited by the number of samples and lack of estimates by previous studies. However, this matches our existing trend in across our multiple datasets showing Lemon having a notable, but still lesser than Paradise, geothermal component. Furthermore, Barrett and Pearl use Na-K-Ca geothermometers to estimate a range of ~190-210 at Lemon Spring. This range is an overestimate due to the presence of travertine interfering with this method, and therefore our estimated range is likely, given this adjustment.

Near-surface Pathways for Volatiles at the Rico Hot Springs

Based upon the CO_2 flux transects measured at Rico (Fig. 10), we make several interpretations about the pathways for CO_2, and by extension the mantle helium it carries, in the Rico area. Significant increases in flux are observed on both the eastern and western transects across the Last Chance fault trace which confirms the accuracy of the inferred fault location. This fault likely has little cementation and/or a high fracture density associated with its damage zone that maintain high permeability to allow for the elevated flux rates measured across this structure. Travertine is precipitated along geothermal fluid pathways as CO_2 degasses (Crossey, 2009) and is also an expression of high CO_2 flux at spring vents. Several high CO_2 flux locations are not along previously mapped faults; for these, we speculate the presence of potential cryptic basement faults that acted as transfer zones between other faults as shown in Figure 16.

Figure 16 expands on these interpretations of flux data by inferring new fault locations that may better explain our observed CO_2 flux trends. The first of these is the Nellie Bly fault, because no elevated flux is seen along its previously inferred trace except at the point source of Rico Hot Spring #3. Therefore, we interpret the actual

location of this fault to be slightly south such that it aligns with the elevated flux zones on both transects. The zone of most elevated flux within the sample area occurring on only the eastern transect indicates that the structure at this location is more complex than just E-W structures. One possible interpretation of this data is a splay fault trending NW from the Last Chance to Nellie Bly fault, connecting through Rico Hot Springs #1 and #2. The exact geometry could be further resolved with further flux data collection and/or through structural analysis or shallow geophysics.

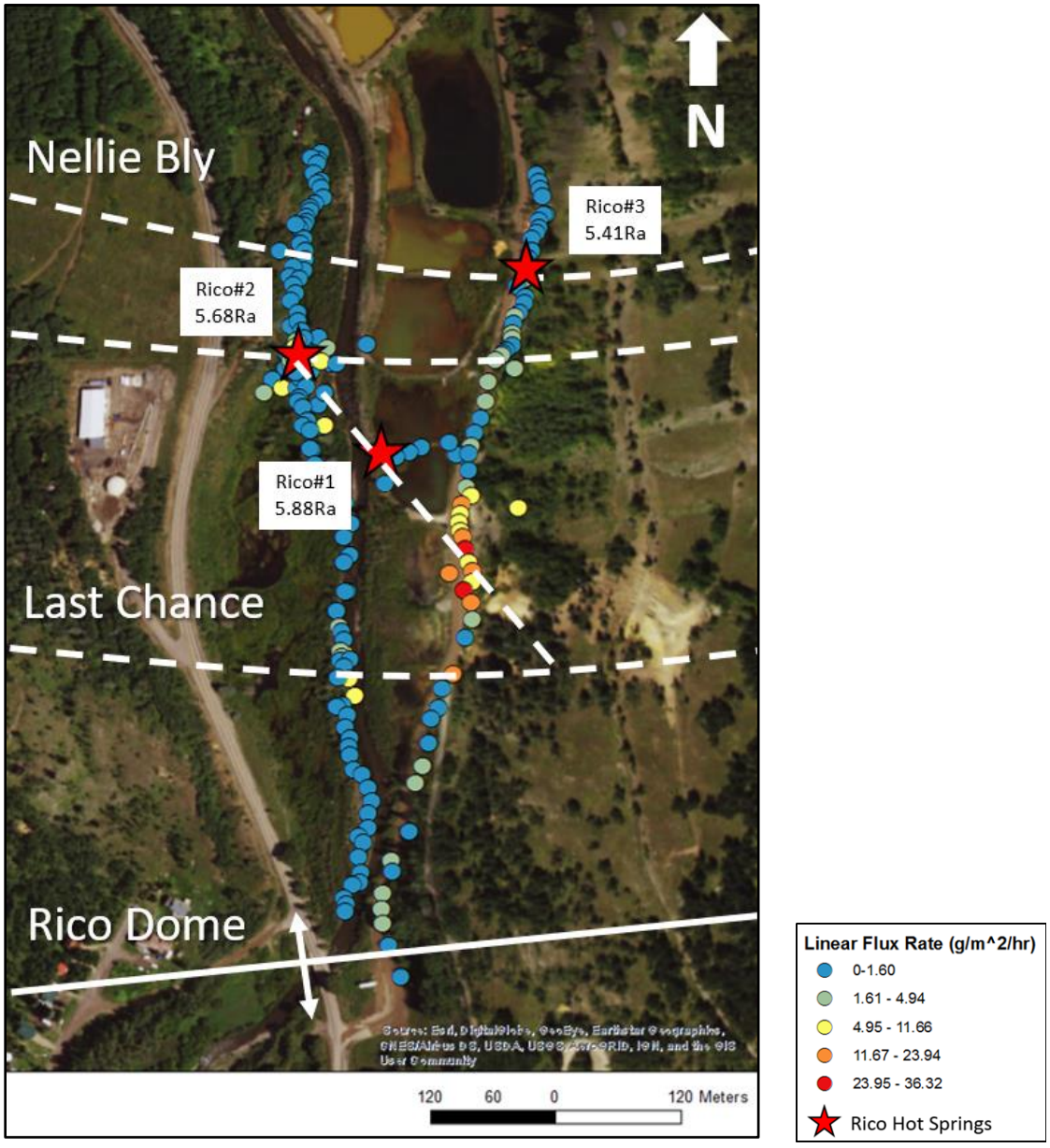

Figure 16. CO_2 flux transects with refined location of the Nellie Bly Fault and speculative trace of splay fault connecting the highest surface flux zones between the Last Chance and Nellie Bly Faults.

Conclusions

This project used multiple-tracer approach to expand our existing datasets of water chemistry, gas chemistry, and surface CO_2 flux of WSJ springs with elevated mantle signature in order to enhance our understanding of mantle-surface connections in continental settings.

First, 14 new noble analyses, paired with tomography, demonstrates that the primary control on elevated mantle gas at surface springs is proximity to low-mantle velocity domains. In this way, we see that mantle volatiles in WSJ Springs are sourced in the asthenosphere from mantle degassing and then transported subvertically through the lithosphere into the groundwater system.

Second, elevated flux along structural pathways at Rico demonstrates that faults are the primary conduits for volatile transport in the near surface. These transects proved to be an effective tool for refining mapping of faults and detection of structural features that lack surface expression.

Third, hydrochemical data reveal that WSJ springs are predominantly meteoric by volume, with a couple springs having a minor but potent component of geothermal brines. There are distinct geochemical signatures for each spring that we attribute to variable water-rock interactions.

Chemical geothermometry suggests a wide range of reservoir temperatures. Paradise and Lemon exhibit reservoir temperature estimates up to 180 °C that make them promising candidates for energy development. Even Rico, with somewhat lower estimates, may have potential for further geothermal exploration.

Collectively, these findings lead us to a general model of the mantle-to-surface conduit system observed in the WSJ Mountains. Tomography reveals an asthenospheric source of mantle gases (CO_2 and ^3He). Continued subvertical transport of these volatiles through the lithosphere is documented in the region by young volcanism, elevated $^3He/^4He$ levels at geothermal springs, and degassing of endogenic CO_2 along structural features associated with these springs. Upper crustal conduits for volatiles include fault zones because of inherited permeability and potentially as maintained by neotectonic

activity. Hydrochemical analyses demonstrated that regional springs are sourced by meteoric waters rapidly circulating along isolated flowpaths at depth. The deeply-sourced volatiles travel upwards along structures and interact with the meteoric fluids as they are heated at depth. Gas-enriched fluids rise along regional structures and reach surface springs. Collectively, this project enhances our understanding of mantle-to-surface connections in this prominent geothermal system.

References Cited

Andrews, J.N., 1985, The isotopic composition of radiogenic helium and its use to study groundwater movements in confined aquifers: Chemical Geology, v. 49, p. 339–351.

Barrett, J.K., and Pearl, R.H., 1976, Hydrogeological data of thermal springs and wells in Colorado: Information Series 6: Denver, CO, Colorado Geological Survey, 124 p.

Barrett, J.K., and Pearl, R.H., 1978, An appraisal of Colorado's geothermal resources: Colorado Geological Survey Bulletin 39, p. 224

Boles, J. R., Garven G., Camacho, H., and Lupton , J.E., 2015, Mantle helium along the Newport-Inglewood fault zone, Los Angeles basin, California: A leaking paleo-subduction zone: Geochemistry, Geophysics, Geosystems, v. 16, p. 2364–2381, doi:10.1002/2015GC005951.

Bush, A.L., and Bromfield, C.S., 1966, Geologic map of the Dolores Peak quadrangle, Dolores and San Miguel Counties, Colorado: U.S. Geologic Survey Geologic Quadrangle Map GQ-536

Bush, A.L., Bromfield, C.S., and Pierson, T.L., 1956, Preliminary geologic map of the Placerville quadrangle, Colorado: U.S. Geologic Survey Mineral Inv. Field Studies Map MF-96

Chiodini, G., Cioni, R., Guidi, M., Raco, B., and Marini, L., 1998, Soil CO2 flux measurements in volcanic and geothermal areas: Applied Geochemistry, v. 13, no. 5, p. 543-552.

Chiodini, G., Baldini, A., Barberi, F., Carapezza, M.L., Cardellini, C., Frondini, F., Granieri, D., and Ranaldi, M., 2007, Carbon dioxide degassing at Latera Caldera (Italy): Evidence of geothermal reservoir and evaluation of its potential energy: Geophysical Research, v. 112, p. 17

Clarke, W.B., Beg, M.A., and Craig, H., 1969, Excess 3He in the sea: Evidence for terrestrial primordial helium: Earth and Planetary Science Letters, v. 6, p. 213–220, doi:10.1016/0012 -821X(69)90093-4.

Craddock, W.H., Blondes, M.S., DeVera, C.A., Hunt, A.G., 2017, Mantle and crustal gases of the Colorado Plateau: Geochemistry, sources, and migration pathways: Geochimica et Cosmochemica Acta, v. 21, p. 346-374

Crossey, L.J., Karlstrom, K.E., Springer, A., Newell, D., Hilton, D., and Fischer, T., 2009, Degassing of mantle-derived CO2 and 3He from springs in the southern Colorado Plateau region—Neotectonic connections and implications for groundwater systems: Geological Society of America Bulletin, v. 121, p. 1034–1053, doi:10.1130 /B26394.1.

Crossey, L.J., Karlstrom, K.E., Schmandt, B., R.R. Crow, Colman, D.R., Cron, B., Takacs-Vesbach, C.D., Dahm, C.N., Northup, D.E., Hilton, D.R., Ricketts, J.W., Lowry,

A.R., 2016, Continental smokers couple mantle degassing and distinctive microbiology within continents: Earth and Planetary Science Letters, v. 435, p. 22-30.

Curewitz, D. and Karson, J.A., 1997, Structural settings of hydrothermal outflow: Fracture permeability maintained by fault propagation and interaction: Journal of Volcanology and Geothermal Research, v. 79, p. 149-168, http://dx.doi.org/10.1016/S0377-0273(97)00027-9.

Davis, S.N., Whittermore, D.O., Fabryka-Martin, J., Uses of chloride/bromide ratios in studies of potable water: Groundwater, v. 36, no. 2, p. 338-350

Easley, E. and Morgan, P., 2013, Fluid, Gas, and Isotopic Variation of Thermal Springs in the Southern Rocky Mountains: Colorado: GRC Transactions, v. 37, p. 385

Embley, R.W., Chadwick, W.W., Jonasson, I.R., Butterfield, D.A., and Baker, E.T., 1995, Initial Results of the Rapid Response to the 1993 Coaxial Event: Relationships Between Hydrothermal And Volcanic Processes: Geophysical Research Letters, v. 22, p. 143–146.

Fournier, R.O., 1977, Chemical geothermometers and mixing models for geothermal systems: Geothermics, v. 5, p. 41-50.

Fournier, R.O., 1979, A revised equation for the Na/K geothermometer, Geothermal Resources Council Transactions, v. 3, p. 221-224.

Fournier, R.O. and Potter, R.W. II, 1979, Magnesium correction to the Na-K-Ca geothermometer: Geochimica Cosmochimica Acta, v. 343, p. 1543-1550.

Fournier, R.O. and Potter, R.W. II, 1982, A revised and expanded silica (quartz) geothermometer: Geothermal Resource Council Bulletin, V. 11, p. 3-9.

Fournier, R.O., and Truesdell, A.H., 1973, An empirical Na-K-Ca geothermometer for natural waters: Geochimica Cosmochimica Acta, v. 37, p. 155-1275.

Fournier, R.O., White, D.E., and Truesdell, A.H., 1974, Geochemical indicators of subsurface temperature - 1. Basic assumptions.: United States Geological Survey Journal of Research, v. 2, p. 259-262

Gautheron, C., and Moreira, M., 2002, Helium signature of the subcontinental lithospheric mantle: Earth and Planetary Science Letters, v. 199, p. 39–47, doi:10.1016/S0012-821X(02) 00563-0.

Giggenbach, W.F., 1988, Geothermal solute equilibria: Geochimica Cosmochimica Acta, v. 52, p. 2749-2765.

Gonzales, D.A., 2015, New U-Pb Zircon and 40Ar/39Ar age constraints on the late Mesozoic to Cenozoic plutonic record in the Western San Juan Mountains: The Mountain Geologist, v. 52, no. 2, p. 5-42

Gonzales, D.A. and Lake, E.T., 2017, Geochemical constraints on mantle-melt sources for Oligocene to Pleistocene mafic rocks in the Four Corners region, USA: Geosphere, v. 13, no. 1, p. 201-226

Graham, D.W., 2002, Noble gas isotope geochemistry of mid-ocean ridge and ocean island basalts: Characterization of mantle source reservoirs, in Porcelli, D., Ballentine, C.J., and Weiler, R., eds., Reviews in Mineralogy & Geochemistry—Noble Gases in Geochemistry and Cosmochemistry: Washington, D.C., Mineralogical Society of America, v. 47, p. 481–538.

Hoke, L., Poreda, R., Reay, A., Weaver, S.D., 2000, The subcontinental mantle beneath southern New Zealand, characterized by helium isotopes in intraplate basalts and gas-rich springs, Geochimica et Cosmochimica Acta, v. 64, no. 14, pp. 2489-2507

Hou, X., and Jones, B.T., 2000, Inductively coupled plasma/optical emission spectrometry: Encyclopedia of Analytical Chemistry, p. 9468–9485

Jackson, P.E., 2000, Ion chromatography in environmental analysis: Encyclopedia of Analytical Chemistry, p. 2779-2801

Kamensky, I. L., Tolstik I.N., and Vetrin V.R., 1990, Juvenile helium in ancient rocks: I. 3He excess in amphiboles from 2.8 Ga charnokite series—Crust-mantle fluid in intercrustal magmatic processes: Geochimica et Cosmochimica Acta, v. 54, p. 3115–3122. 17

Karlstrom, K.E., Crossey, L.J., Hilton, D.R., and Barry, P.H., 2013, Mantle 3He and CO2 degassing in carbonic geothermal springs of Colorado and implications for neotectonics of the Rocky Mountains: Geology, v. 41, p. 495 – 498 Lewicki, J.L. and Brantley, S.L., 2000, CO2 degassing along the San Andreas fault, Parkfield, California: Geophysical Research Letters, v. 27, no. 1, p. 5-8.

Larson, P.B., Cunningham, C.G., and Naeser, C.W., 1994a, Large-scale alteration effects in the Rico paleothermal anomaly, southwestern Colorado, Economic Geology, v. 89, p. 1769-1779

Larson, P.B., Cunningham, C.G., and Naeser, C.W., 1994b, Hydrothermal alteration and mass exchange in the hornblende latite porphyry, Rico, Colorado: Contributions to Mineralogy and Petrology, v. 116, p. 119-215

Luedke, R.G., Burbank, W.S., 1962, Geologic map of the Ouray quadrangle, Colorado: U.S. Geological Survey Geologic Quadrangle Map GQ-192

Lupton, J. E., 1983, Terrestrial inert gases: Isotope tracer studies and primordial components in the mantle: Annual Review of Earth and Planetary Science, v. 11, p. 371–414.

Martel, S.J. and Peterson, J.E., 1991, Interdisciplinary Characterization of Fracture Systems at the US/BK Site, Grimsel Laboratory, Switzerland: International Journal of Rock Mechanics and Mining Sciences & Geomechanics, v. 28, no. 4, p. 295-323

Martini, M., 1984, On the behaviour of fluorine in volcanic processes: Bulletin Volcanologique, v. 47, p. 483-489. doi:10.1007/BF01961220

Marty, B., and Jambon, A., 1987, C/3He in volatile fluxes from the solid Earth: Implications for carbon geodynamics: Earth and Planetary Science Letters, v. 83, p. 16–26.

McKnight, E.T., 1974. Geology and ore deposits of the Rico District, Colorado: US Geological Survey, Professional Paper 723, p. 1 – 100.

Michalowski, T. and Asuero, A.G., New Approaches in Modeling Carbonate Alkalinity and Total Alkalinity: Critical Reviews in Analytical Chemistry, v. 42, p. 220-244

Minor, S.A., and Hudson, M.R., 2006, Regional survey of structural properties and cementation patterns of fault zones in the northern part of the Albuquerque Basin, New Mexico—Implications for groundwater flow: U.S. Geological Survey Professional Paper 1719, 28 p.

Mutschler, F.E., Larson, E.E., and Bruce, R., 1987, Laramide and younger magmatism in Colorado, Col. School Mines Quart., v. 82, pp. 1–45, 1987.

Newell, D.L., Crossey, L.J., Karlstrom, K.E., Fischer, T., and Hilton, D.R., 2005, Continental-scale links between the mantle and groundwater systems of the western United States: Evidence from travertine springs and regional He isotope data: GSA Today, v. 15, no. 12, p. 4–10, doi: 10.1130/1052- 5173(2005)015[4:CSLBTM]2 .0.CO;2. Piper, A.M., 1944, A Graphic Procedure in the Geochemical Interpretation of Water Analysis: American Geophysical Union, Transactions, v. 25, is. 6, p. 914-928. 18

Nicholson, Keith, 1993, Geothermal fluids: chemistry and exploration techniques. Berlin; New York : Springer-Verlag, p. 19-50

Oerter, E.J., 2011, Geothermometry of thermal springs in the Rico, Dunton, and West Fork Dolores River areas, Dolores County, Colorado: Colorado Geological Survey Department of Natural Resources

Powell, T., and Cumming, W., 2010, Spreadsheets for geothermal water and gas geochemistry: Proceedings, 35th Workshop on Geothermal Reservoirs, Engineering, Stanford University, Stanford, CA: SGP-TR-188.

Pratt, W.P., McKnight, E.T., and DeHon, R.A., 1969, Geologic map of the Rico quadrangle, Colorado: U.S. Geological Survey Geologic Quadrangle Map GQ-797 Sano, Y., and Marty, B., 1995, Origin of carbon in fumarolic gas from island arcs: Chemical Geology, v. 119, p. 265-274.

Ricketts, J.W., Kelley, S.A., Karlstrom, K.E., Schmandt, B., Donahue, M.S., and Van Wijk, J., 2016, Synchronous opening of the Rio Grande rift along its entire length at 25–10 Ma supported by apatite (U-Th)/He and fission-track thermochronology, and evaluation of possible driving mechanisms: GSA Bulletin, v. 128; no. 3/4; p. 397–424

Schmandt, B., and Humphreys, E. D., 2010, Complex subduction and small-scale convection revealed by body-wave tomography of the western U.S. upper mantle: Earth and Planetary Science Letters, v. 297, p. 435–445, doi:10.1016/j.epsl .2010.1006.1047.
Smith, J., 2016, CO2 flux along faults of the central Rio Grande rift, New Mexico [Master Thesis]: University of New Mexico

Shevenell, L., Goff, F., Vuataz, F., Trujillo, P.E. Jr, Counce, D., Janik, C.J., Evans, W., 1987, Hydrogeochemical data for thermal and nonthermal waters and gases of the Valles Caldera – Southern Jemez Mountains region, New Mexico: Los Alamos National Laboratory Report, LA-10923-OBES

Smith, M., Bisiar, T., Putra, T. and Blackwood, V., 2011. Geochemistry of geothermal fluids Rico, Colorado. Final report: 22p.

Tan, H., Chen, J., Rao, W., Zhang, W., Zhou, H., 2012, Geothermal constraints on enrichment of boron and lithium in salt lakes: An example from a river-salt lake system on the northern slope of the eastern Kunlun Mountains, China: Journal of Asian Earth Sciences, v. 51, p. 21-29 USGS, 2006, National field manual for the collection of water-quality data, U.S. Geological Survey Techniques of Water-Resources Investigations: book 9, chaps. A1-A9, Volume 2006, USGS.

Thomas, W.A., 2007, Pennsylvanian sinistral faults along the southwest boundary of the Uncompahgre uplift, Ancestral Rocky Mountains, Colorado: Geosphere, v. 3, p. 119-132

Vuataz, F.D., and Goff, F., 1986, Isotope geochemistry of thermal and nonthermal waters in the Valles Caldera, Jemez Mountains, Northern New Mexico: Journal of Geophysical Research, v. 91, no. B2, p. 1835-1853

Werner, C., Hurwitz, S., Evans, W. C., Lowenstern, J. B., Bergfeld, D., Heasler, H., Jaworowski, C., Hunt, A., 2008, Volatile emissions and gas geochemistry of Hot Springs basin, Yellowstone National Park, USA: Journal of Volcanology and Geothermal Research, v. 178, p. 751-762.

White, A.F., Delaney, J.A., Truesdell, A.F., Janik, C., Goff, F., and Crecraft, H., 1984, Fluid chemistry of the Baca geothermal field, Valles Caldera, New Mexico: Field Conference Guidebook NM Geological Society, v. 35, p. 257-263

Whyte, C., Karlstrom, K.E., Crossey, L.J., Gonzales, D.A., Darrah, T.H., 2016, Evaluating mantle-crustal gas dynamics of Southwestern US CO2 springs using helium isotopes and heavy noble gases: Geological Society of America Abstracts with Programs, v. 48, no. 7.